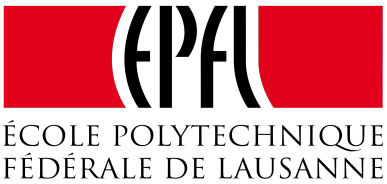


# Remote-sensing and classification of benthic landscapes for satellite derived bathymetry

**Sélim Amrari**

Master thesis

February, 2018

Supervisors :

Dr. Hugues Lemonnier, Romain Le Gendre, Benoit Soulard
LEADNC, IFREMER - New Caledonia

Prof. Dr. Alfred Johny Wüest
Physics of Aquatic Systems Laboratory, EPFL - Switzerland

# Abstract

Bathymetry is a crucial variable for many researches, such as hydrodynamics of coastal areas, species distribution modeling, sea-level rise induced, sedimentology studies. In coral ecosystems, knowledge about depth is crucial as it controls, jointly with water quality and light penetration throughout the water column. Traditional bathymetric measurements are made by echo-sounder, a type of sonar either mono or multi-beam, measuring water depth from sea surface. Nevertheless, this acquisition process remains expensive and cannot be applied everywhere. Despite less accurate results, passive satellite derived bathymetry can provide a large-scale resolution at a lower cost. This study explores the potential of empirical models applied on images provided by Sentinel-2 sensor for bathymetry retrieval. Technical issues and suitable conditions are described here. In addition, a different approach is proposed. It is composed of an initial step designed to classify areas relying on their bottom reflectance and their water optical properties. Tests are achieved in New Caledonia, in the South West part of the lagoon. The method showed its ability to produce bathymetric data at a large scale, including shallow coral areas, which may be difficult to measure by boat. The proposed approach allowed to improve the results of traditional empirical models. For this reason, satellite derived bathymetry can provide a valuable alternative for knowledge of unmapped coral reefs areas.

# Contents

# List of Figures



# List of Tables

# 1 Introduction

## 1.1 New Caledonian Lagoon

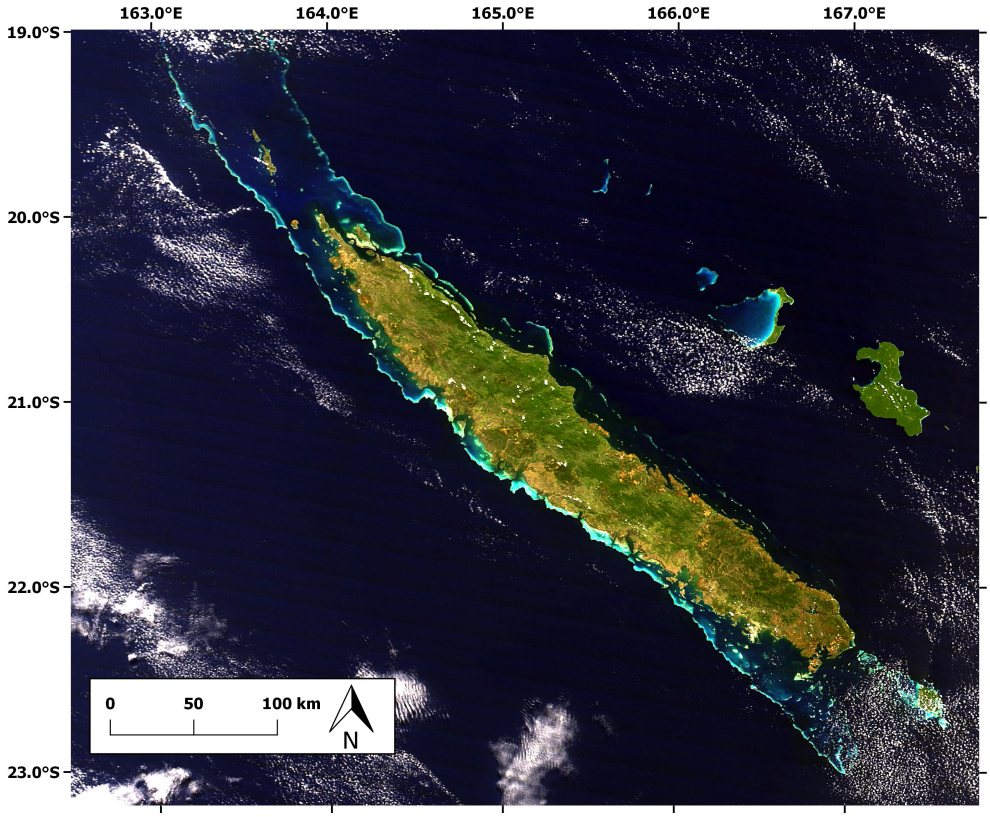


**(a)** Image acquired on September 24, 2012 above New Caledonia by Moderate Resolution Imaging Spectroradiometer (MODIS) on NASA's Terra satellite

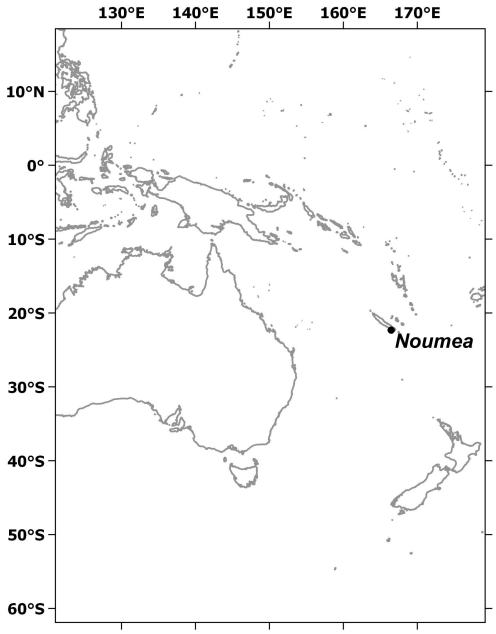


**(b)** Global situation

**Figure 1:** Satellite image and localization of New Caledonia

New Caledonia is located at approximately 1500 km east of Australia, in the South Pacific Ocean. The main island, called "Grande Terre" is a mountainous and elongated land of approximatively 400 km long and 40 to 70 km wide. This island is surrounded by barrier reefs which are forming the second largest coral reef area in the world. Due to its highly diverse and healthy coral ecosystems, New Caledonia lagoons have been added to the UNESCO World Heritage List in 2008. Reef cover a total of 4'537 $km^2$, whereas non-reef areas such as lagoons, enclosed basins, inlets and terraces cover 37'336 $km^2$ [Andrefouet et al., 2009]. The south-west part of this lagoon is a wider, semi-open coral reef lagoon, surrounded by intertidal barrier reefs with several deep inlets [Ouillon et al., 2010].

New Caledonia experiences a dry-tropical regime, with transitions between dry and wet seasons, respectively from June until September and from December until April. Its climate is characterized by south-easterly trade winds, sudden and heavy rainfall, cyclones, swell incoming irregularly from south or south-east and torrential hydrological regime. Furthermore, it can undergo seasonal variations due to El Niño Southern Oscillation (ENSO) [Ouillon et al., 2010].

The New Caledonian Lagoon receives different inputs from rivers and ocean. Inputs of oceanic waters are mainly incoming through the South part of the lagoon which is semi-open and widely open at its eastern location. River inputs can be considerable during heavy-rain events, leading to high sediment inputs during the following days. However, sediment inputs are very low in the absence of heavy rains [Ouillon et al., 2010] which may provide suitable conditions for satellite derived bathymetry. Variations of sedimentation inlets and concentration of suspended particle matters, are finally driven by the effects of tide, wind, precipitations and swells. Reef communities undergoes damaging effects due to the abrasive capacity and the reduction in light penetration caused by suspended particles. Damages such as bleaching can also be enhanced by storms. In addition, New Caledonia has large scale mining factories, involving soil extraction and thus inducing erosion, which lead to an increase of sedimentary fluxes.

This situation enforces the need for effective monitoring and knowledge acquisition about lagoon geomorphology, dynamics and processes.

## 1.2 Research background and motivation

This work takes part of a major research project named PRESENCE, "PREssions sur les Ecosystèmes récifo-lagonaires de Nouvelle-CalédoniE", aims at studying long-term effects of pressures on coral and lagoon ecosystems of New Caledonia. Main tool of the project are hydrodynamic modeling, remote-sensing and monitoring of the quality of water bodies.

A better understanding the lagoon's processes is a primary necessity in order to monitor pressures and stress due to seasonal and anthropological effects or extreme weather events. Hydrodynamics models are of primary interest for investigating dynamics and fate of terrestrial inputs into New Caledonian Lagoons. For such models, knowledge about the interfaces (e.g. boundary conditions) is crucial. Oceanic and atmospheric boundaries usually come from regional numerical model whereas locally refined grid uses the highest bathymetric dataset available. Moreover, realism of models' outputs is also strongly influenced by the quality of the bathymetric grid. Lastly, knowing the bathymetric landscape of coral area is very important. It may allow to estimate its vulnerability to storm events or to global warming. Additionally, lagoon of New Caledonia contains many gap of bathymetric data within pristine areas such as "chesterfield", "Bellona", "Pétrie", "Astrolabe" or "Entrecasteaux".

Traditionally, bathymetric measurements are made by echo-sounder, a type of sonar, either mono or multi-beam, measuring water depth from sea surface. Nevertheless, this acquisition process remains expensive regarding the means and time required for mapping a defined area. Furthermore, these methods are often not achieved on shallow depth areas, where boats can hardly sail. Methods relaying on bathymetric LIDAR from airborne are also possible but still expensive [Duplancic Leder, 2017]. Despite less accurate results, satellite derived bathymetry can provide a large scale water depth retrieval with high resolution at a lower cost [Wang and Philpot, 2007]. However, it requires some specific environmental conditions such as clear water, cloud-free sky, calm waters and some specific sensor conditions, such as good penetrating abilities of its wavelength or a zenith angle of the view angle of the sensor.

## 1.3 Physical principles in water surrounding

In order to understand the factor of variation of the signal recorded from the satellite above water area, some basic principles of optical physics have to be reminded.

**Radiance:** The signal, recorded by the satellite sensor, corresponds to the electromagnetic radiation flux which is emitted or reflected by a surface. This signal is dependent on: the area of the source, corresponding to the ground pixel resolution, the view and solid angles of the sensor, the wavelength of the radiation and the irradiance, which is the radiation received by the surface. This recorded radiance signal is described by a digital number attributed to each pixel. Radiance is therefore different from reflectance, which is the ratio of incident electromagnetic power that is reflected by a surface. The spectral signature describes the reflectance properties of a surface for each wavelength.

**Reflection:** Reflection is the change in direction of electromagnetic radiation at a surface. The direction of the reflected radiation varies, depending on the surface roughness. In most cases, reflection is said diffuse, meaning that radiations are reflected in every direction with a stronger component of reflection in a specific direction. This stronger component is resulting from specular reflection. As an example, glass surfaces, which are characterized by really small roughness, exhibit only specular reflection. On the contrary, a surface with perfect equal reflection in every direction is called "Lambertian surface". For instance, the ocean water surface has a strong specular reflection component, which is commonly named as "glint", whereas subsurface bottom surfaces are often much more similar to "lambertian surfaces" .

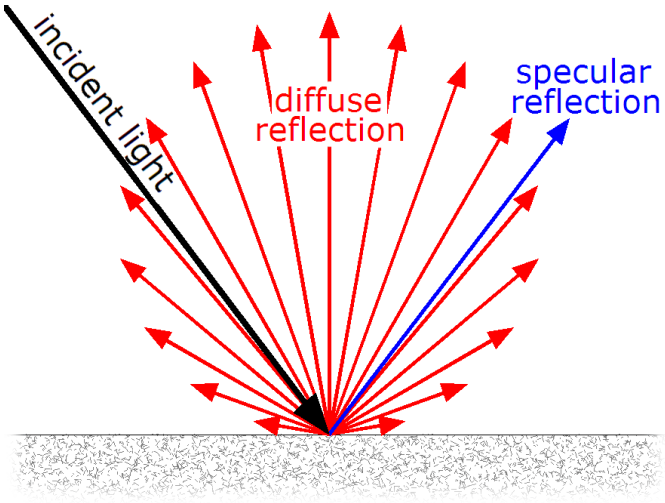


**Figure 2:** Usual reflection on a surface which produces a combination of diffuse and specular reflection (Image taken from wikipedia)

**attenuation:** Electromagnetic radiation undergoes attenuation along its pathway, due to absorption and scattering. Absorption is a molecular process, in which energy of photons that constitutes radiation, are absorbed by the matter. The energy absorbed by the matter can be converted as a temperature rise. Scattering is a process characterized by a change in direction

of radiation's trajectory, due to particles contained in the surrounding medium. This change in direction is strongly dependent on the ratio between the particle size and the radiation wavelength. As a result, attenuation is usually described by a coefficient $k$, dependent on the wavelength. In water, longer wavelengths undergoes stronger attenuation. Volume scattering refers to a sum in scattering process resulting in a throwback of radiation toward the sky, without any reflection on a subsurface bottom. Attenuation is a process occurring in surrounding waters as well as in the atmosphere. The correction of the satellite signal, after estimation of the atmosphere compounds along the pathway, refers to atmospheric correction of the images.

In summary, there are three main subsurface factors of variation of the recorded signal: benthic substrate which is characterized by a bottom reflectance, water compounds influencing optical properties and depth. Finally, simple models of the radiance can be achieved with $R$, the total subsurface reflectance, $h$, the water depth, $L^-$, the upwelling radiance, $E^-$, the downwelling irradiance, $L_s$, the water radiance induced by volume scattering in an infinitely deep water-column, $L_b$, the radiance induced by subsurface bottom and $k$, the sum of the diffuse attenuation coefficients for upwelling and downwelling radiation [Lyzenga et al., 2006]. However, the form of this solution does not take into account some processes such as internal reflection, at the air-water interface, of the upwelling radiance back downward. Furthermore, it is only valid for close to zenith solar and view angle.

$$R = \frac{\pi L^-}{E^-} \tag{1}$$

$$L(h) = L_s + L_b e^{-kh} \tag{2}$$

## 1.4 State of the art: satellite derived bathymetry

Methods relying on passive remote sensing can be divided into different categories including: empirical modeling, semi-analytical physic-based modeling, machine-learning approaches or even pure classification.

Most of the empirical methods rely on a simplified model to approximate the radiative transfer solutions through water surfaces of shallow areas [Lyzenga et al., 2006, Lyzenga, 1978]. As it is developed in section 1.3, these simplified models introduce an exponential relationship between water depth and attenuation of the radiation. Empirical methods are easier to apply but require empirical calibration of parameters making in-situ measurements necessary. But there are some disadvantages: they also suppose strong assumptions such as homogeneity of water column and its optical properties. They do not allow any relationship across sensors [Dekker et al., 2012]. However, they have one strong advantage : their performances remain good without atmospheric correction. Coastal atmospheric correction on multi-spectral images, composed of few bands for estimating atmospheric compounds, is indeed a really hard task. Casal et al. [2017] compared the application, on Sentinel-2 images, of empirical methods with and without atmospheric correction. Results show equivalent performance with Lyzenga's method (see section 2.7.1) and lower performance of atmospherically corrected image with Stumpf's method (see section 2.7.2). Currently, empirical methods based on regression remain the most widely used [Manessa et al., 2016].

Instead of empirically calibrating unknown parameters, physic-based modeling consists in optimizing more constrained systems of equations describing spectral attenuation along radiation pathways [Hamylton et al., 2015]. The optimized variables are restricted within ranges based on knowledge of typical water compositions. In contrast with empirical methods, water properties are assumed to be variable among the pixels. Constrained system of equations is therefore optimized for describing at best the reflectance of each pixel. Consequently, these methods are not concerned by any assumption of homogeneity. They do not require in-situ measurements and, after atmospheric corrections, their outputs can easily be merged across different sensors [Dekker et al., 2012]. Using airborne hyperspectral imagery, they seems to provide much better results than empirical methods [Dekker et al., 2011]. However, they require an accurate atmospheric correction in order to find a correspondence between modeled reflectance pixels and observed pixels corrected from atmospheric effects. Despite a use on simulated multi-spectral satellite data [Hedley et al., 2012], their applications remain on development on proper multi-spectral satellite sensors.

With the increase of computational power, predictive modeling tends to propose solutions in a wide range of domains. The scope of the techniques proposed by machine-learning generally gets rid of any research of physical explanation. They only intend to train a model, based on a generic configuration chosen by the user, by optimizing generalization error (defined in section 2.8.1). In satellite derived bathymetry, Artificial Neural Networks (ANN) appeared to provide a suitable structure for the evaluation of non-linear relationships between spectral radiances and depth [Ceyhun and Yalçın, 2010]. Therefore, the use of different combinations of wavelengths theoretically allows to isolate water attenuation and depth from environmental factors such as bottom material [Hassan et al., 2015]. In 1998, ANN models already demonstrated their ability to predict artificial reflectances dataset generated by Lee's algorithm from 0.5 to 20 m depth [Lee et al., 1998b]. Lately, ANN with simpler networks have achieved good performance in comparison with empirical algorithm during experiments located in the Caribbean Sea and the Hawaiian Sea [Liu et al., 2015].

Simultaneous supervised classifications of bottom depths and benthic substrates of Australian reef, have also been demonstrated from satellite sensor, Hyperion. After atmospheric correction, benthic substrates classification is achievable up to the coral species using techniques of spectral signatures matching [Kutser and Jupp, 2006, Kutser et al., 2006, 2003]. Random forest methods have also been used to describe the non-linear relation between pixel radiance and water depth in case of water optical properties and bottom type variation [Manessa et al., 2016].

Table 1, shows a brief summary of case studies, observed in the scientific literature. The most used methods with multi-spectral data, rely on empirical modeling. Their performances provide ranges of mean absolute errors from 1 meters to 3 meters. This errors, in percent, usually lie around 40 %. However, on shallow depth, mean absolute error in percent can strongly increase. The maximum predictable depth with empirical models is variable among areas. Currently, semi-analytical physic-based modeling is often used with hyperspectral data and offers accurate depth predictions in case of good conditions and pretreatments such as atmospheric corrections. Attempt of machine-learning approaches rely most of the time on ANN and provide variable results. Their results are often not fully explainable. At that point, the present work mainly focuses on empirical methods.

| Areas, References | Satellite/airborne Data | Methods | Performances and comments |
|---|---|---|---|
| Cancun<br>Duck, Nc<br>Kahana Bay, HI<br>Carysfot Reef, FL<br>Pearl Harbor, HI<br>Honolulu, HI<br>Diamond Head, HI<br>Maunaloa Bay, HI<br>[Lyzenga et al., 2006] | Ikonos | Lyzenga's model | Bathymetry up to:<br>Minimum 10 m (Duck)<br>Maximum 25 m (MaunaLoa)<br>Mean absolute error :<br>Minimum 1.65 m (Cancun)<br>Maximum 3.02 m (Pearl H.) |
| Pearl and<br>Hermes Reef, HI<br>Kure Atoll, HI<br>[Stumpf et al., 2003] | Ikonos | Stumpf's model<br>Lyzenga's model | Both methods are limited to 15 m in case of high turbidity<br>Ratio transform:<br>Has superior depth penetration ability<br>Relevant for more benthic habitats<br>Undergoes an increased level of noise<br>Up to 25 m, mean abs. error: 30%<br>Linear transform:<br>Better ability to resolve fine morphology<br>Up to 15 m, mean abs. error: 50% |
| Heron reef,<br>Australia<br>[Hedley et al., 2009] | hyperspectral airborne<br>sensor : CASI (17 bands) | Lee's model<br>with: ALUT,<br>Levenberg-Marquardt | Bathymetry up to 20 meters<br>Mean absolute error :<br>ALUT: 0.773 m<br>L.-M.: 0.901 m |
| Heron reef,<br>Australia<br>[Hedley et al., 2012] | Simulated from CASI:<br>SPOT -4,<br>L. ETM+,<br>Sen2 | Lee's model<br>with ALUT | Bathymetry up to 20 meters (with Sen2)<br>Out-performance of Sen2 sensor :<br>Best mean absolute error: 0.53 m<br>Improvement factors : additional shortwave blue band, better spectral and spatial resolution |
| West florida shelf,<br>Key west, Fla.,<br>Bahamas<br>[Hedley et al., 2009] | hyperspectral<br>above-water sensor | Lee's model<br>with: non-linear<br>optimization | Bathymetry up to 25 meters<br>Mean absolute error :<br>with turbid water: 1.4 m/10.9%<br>without turbid water: 8.1% |
| Great Barrier reef<br>Australia<br>[Kutser et al., 2006, Kutser and Jupp, 2006, Kutser et al., 2003] | Hyperion | Hydrolight's model<br>with: Supervised<br>classification based<br>on spectral angles | Bathymetry up to 25 meters<br>Maximum absolute error : 1 m<br>Class with maximum error: 1 m |
| Kauai Isl., HI<br>Barbuda Isl.<br>[Liu et al., 2015] | Ikonos<br>L. ETM+ | Neural Net: MLP<br>Lyzenga's model | Best abs error: 1.24 m (MLP)<br>Maximum depth tested: 18 m<br>Out-performance of ANN<br>over Lyzenga's model |
| Foca bay, Tk<br>[Ceyhun and Yalçın, 2010] | Quickbird, Aster | Neural Net: MLP | Best mean abs. error: 7%<br>Bathymetry up to 35 m<br>Suitable to define non-linear relationships between reflectance and depth |

**Table 1:** Synthetic summary of case studies

## 1.5 Aim of the thesis

As seen in section 1.2, bathymetry is a key variable for marine scientists to better apprehend for example hydrodynamics of coral ecosystems or biotopes of benthic organisms. A methodology, adapted to coral ecosystems, allowing a fast bathymetric mapping at large scale could represents a great tool for coastal researchers. It could allow to complete or fulfill missing bathymetric data.

This thesis primary aims at evaluating methods of bathymetry retrieval from passive satellite sensor. This application use images produced by the sensor Sentinel 2. Empirical modeling of the radiometric response to the effect of water attenuation along the radiation pathway is well described in literature. However, regarding the large amount of images and sensors available and the range of variable environmental conditions, bathymetric estimation from passive satellite sensor, remains a difficult task which requires more tests. This work is a direct application of empirical bathymetric models to the multispectral sensor of Sentinel 2. Here, technical issues and procedures applied to the use of these images are described. This study also proposes a different approach, composed of an initial step designed to classify areas relying on their bottom type and their water optical properties. This step aims at isolating variation driven by depth in classes before the selection of one model per classes. The suitable conditions such as the area's scale and the depth's range for an optimal calibration of empirical models are finally investigated.

# 2 Materials and methods

## 2.1 Study site: South part of the New Caledonian Lagoon

The study site for this work is the part of the lagoon situated around Noumea, along the South West coast of New Caledonia. From the "Lepredour Island" at the North of the site to the "Ouen Island" at its South part, this area has an extent of about 2'597 km$^2$. This part of the lagoon is semi-open with four major channels through the barrier reef, named : "Passe De Saint-Vincent", "Passe De Uitoé", "Passe De Dumbéa" and "Passe De Boulari". The south-Eastern part of the site consists in wider openings toward the ocean. The study site is of major interest as it is directly set around the biggest city of the island. Major anthropological effects and strong run-offs through the river can be expected. Several researches also take place in this area. Moreover, the study site is interesting because it offers a great number of in-situ measurements by echo-sounding, which allows to evaluate the ability of the method.

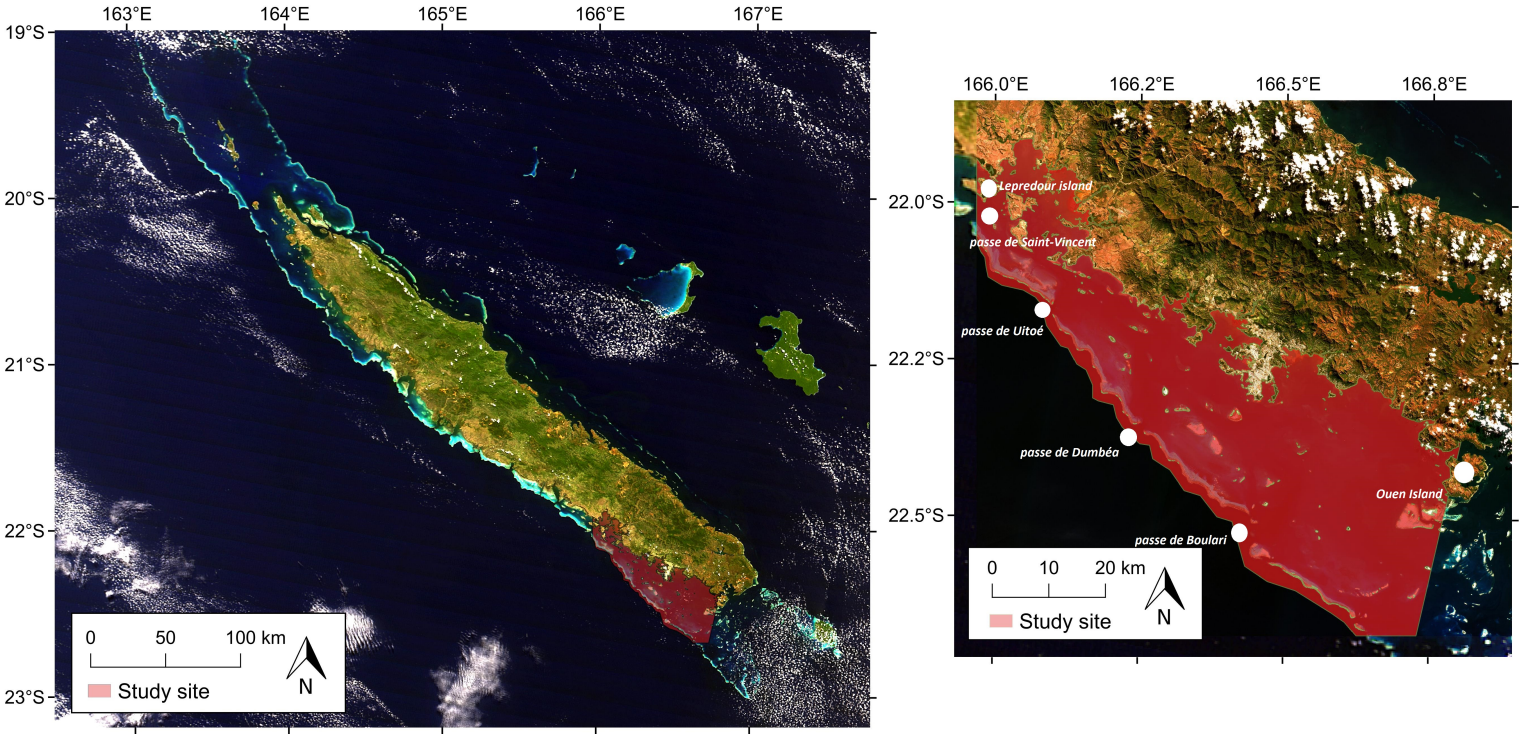


**Figure 3:** Image acquired on September 24, 2012 above New Caledonia by Moderate Resolution Imaging Spectroradiometer (MODIS) on NASA's Terra satellite

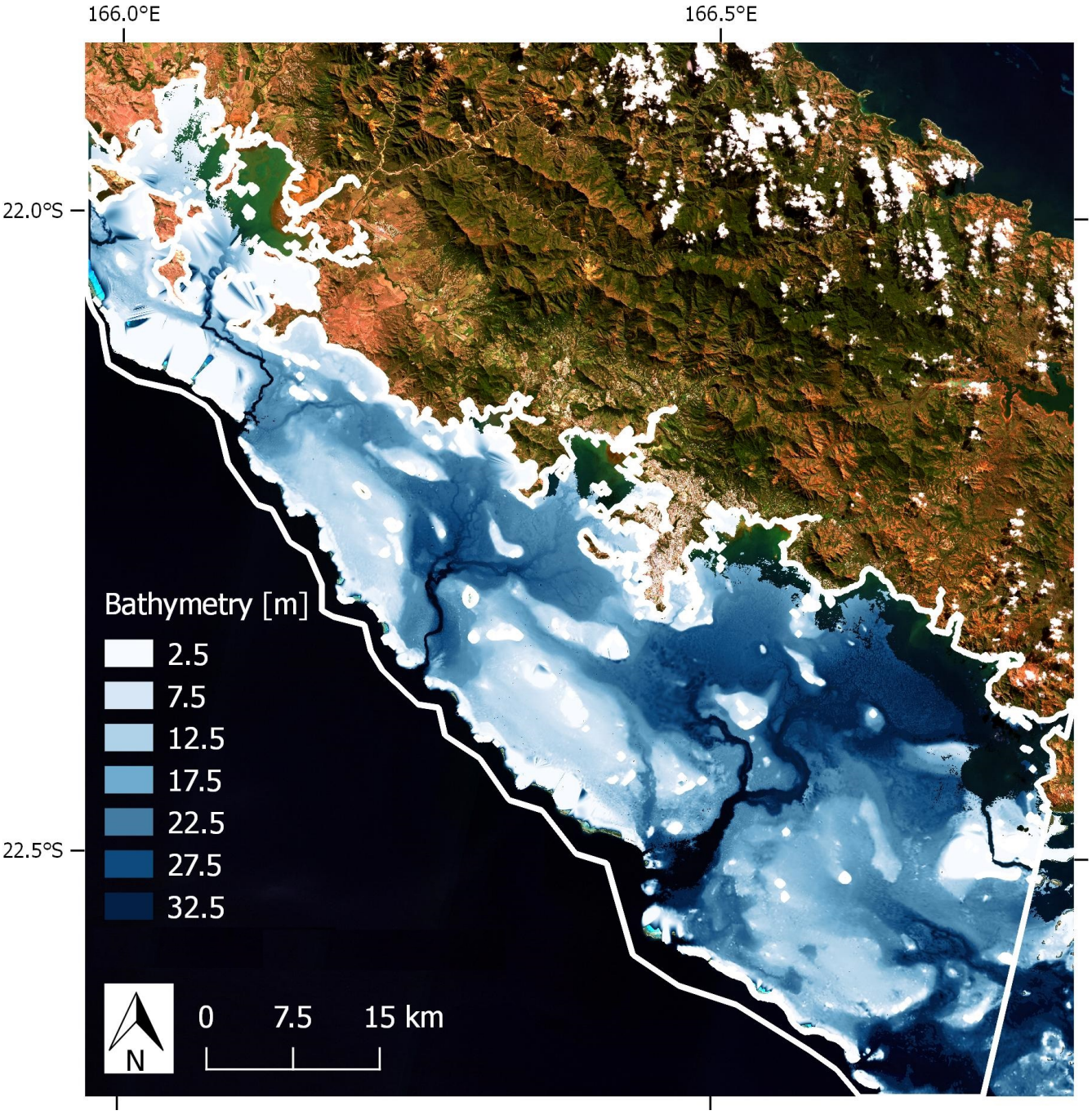


**Figure 4:** Bathymetry produced after interpolation of all in-situ measurements, limited to the surface of prediction. The darkest colors-scale displays depth from 30 meters and more

Figure 4 displays the interpolation of the in-situ measurements, described in section 2.3 within the study site. The study site contains large areas with depths smaller than 30 meters. However deeper zones, such as paleo-valleys connecting passes and bays, also characterize the lagoon.

## 2.2 Satellite sensor: Sentinel-2A

In this work, images provided by satellite Sentinel 2(Sen2) will be used. This choice has distinct advantages. Firstly, the provided data are in open access and the main spatial resolution is about 10 meters without any processing based on panchromatic band. It allows to repeat the analysis on future images and gives to the bathymetric product a good value for money. Secondly, this sensor has an additional blue band with a shorter wavelength. Despite its poor spatial resolution it has a better penetration ability in surrounding waters. Lastly, the 10 meters ground resolution of the usual multi-spectral bands (2, 3 and 4) come in accordance with the need of numerical models. On the other hand, the sensor also comes with disadvantages. In spite of a large swatch width, the sensor is composed of several detectors, set on slightly different view angles. These short differences in the geometries of the detectors' settings result in a visible heterogeneity on the images, visible on Figure 5. preprocessing steps, explained in section 2.4.2, will have to be applied individually on every detector footprint to get rid of this heterogeneity.

| Platform | Sentinel-2A |
|---|---|
| Instrument | Multispectral Imager (MSI) |
| Sensor recording | push-broom |
| Number of detector | 12 |
| Acquisition method | Satellite |
| Coordinate reference system | WGS84 / UTM zone 58s |
| Radiometric resolution [bit/levels] | 12/4095 |
| Temporal resolution [days] | 5 at equator |
| Swath Width [km] | 290 |
| Processing level | Level-1C [1] |

**Table 2:** Sensor details

Table 2 shows the sensor's details. The available images are geometrically corrected and each pixel is characterized by a digital number sampled with 12 bits describing the atmospheric radiance. In this study, bands 1, 2, 3, 4, 5, 8, 8a and 9 are used. Table 3 shows the pixel resolutions and wavelengths of every bands. Bands having a lower spatial resolution are downscaled following bi-cubic interpolation achieved by the use of GDAL package on Python [GDAL Development Team, 201x].

**Table 3:** Wavelengths and Bandwidths of the 3 Spatial Resolutions of the MSI instruments

| Spatial Resolution [m] | Band Number | Central Wavelength [nm] | Bandwidth [nm] |
|---|---|---|---|
| 10 | 2 | 496.6 | 98 |
| | 3 | 560.0 | 45 |
| | 4 | 664.5 | 38 |
| | 8 | 835.1 | 145 |
| 20 | 5 | 703.9 | 19 |
| | 6 | 740.2 | 18 |
| | 7 | 782.5 | 28 |
| | 8a | 864.8 | 33 |
| | 11 | 1613.7 | 143 |
| | 12 | 2202.4 | 242 |
| 60 | 1 | 443.9 | 27 |
| | 9 | 945.0 | 26 |
| | 10 | 1373.5 | 75 |

## 2.3 Bathymetric dataset

In order to calibrate a bathymetric empirical model, in-situ measurements are necessary. To that end, surveys provided by the French National Hydrographic service, SHOM, have been used. These data have been collected since 1965 by echo-sounder with an accuracy of +-2% of depth. The dataset represents 18'556'254 measurements up to 100 meters deep, achieved on the footprint of Sentinel-2A images. Figure 5, shows the setting of the surveys performed above depth up to 30 meters. In our case, regarding the expectation in maximum depth of empirical methods on Table 1, only the measurements up to 30 meters are used.

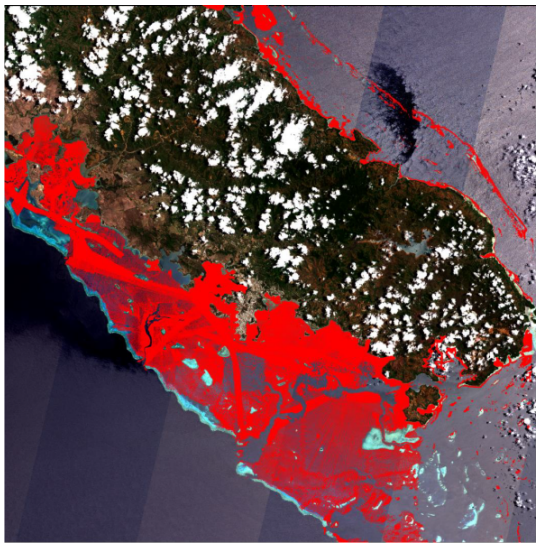

**Figure 5:** Visualization of surveys locations up to 30 meters achieved since 1965, Image acquired on October 31, 2016 above New Caledonia by Sentinel-2A. Surveys' location are scattered in red

## 2.4 Image preprocessing

As explained in section 2.2, images produced by Sentinel-2 result from 12 detectors inducing some disparities between detectors' footprint. These disparities are visible on Figures 6, appearing as linear pattern. Consequently, each preprocessing is achieved on each detectors' footprint individually.

**Figure 6:** Image acquired on October 31, 2016 above New Caledonia by Sentinel-2A

### 2.4.1 Soil and clouds thresholding

In order to properly define the studied area and its corresponding pixels on the image, a first preprocessing step has to be applied to the satellite data. The purpose is to get rid of any pixels which are not describing water surfaces. It is possible to take advantage of the optical properties of water to detect water or wet surfaces on a pixel. As shown in Figure 7, spectral signature of water is extremely low on the near-infrared domain. Therefore, a threshold can, be defined on the band 8 of Sentinel-2 in order to classify the pixels belonging to dry soil at a spatial resolution of 10 meters.

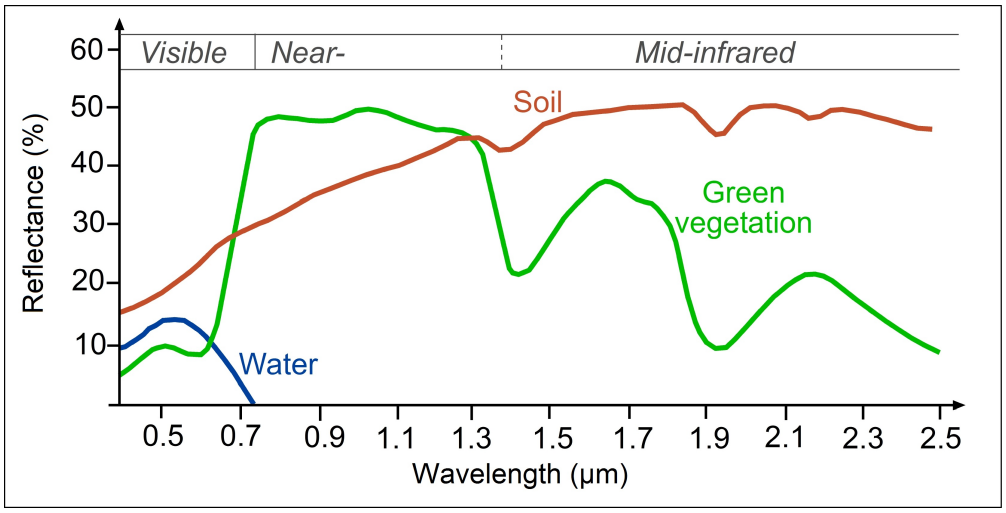


**Figure 7:** Spectral signature of natural surfaces (figure taken from seos-project)

The choice of the thresholding value is not easy, especially regarding the intertidal zone. This zone is defined as the area above water at low tide and under water at high tide. In order to have a similar classification on each detectors' footprint, and to define a suitable value, this threshold has been chosen as quantile computed on the cumulative density frequency curves corresponding to the footprint of every detector.

On the contrary, clouds' spectral signature is extremely high regardless of the wavelength. They can be easily thresholded using the same process as for water applied on several bands (2,3,4 and 8) [Hagolle et al., 2010, Sun et al., 2017].

Figure 8, illustrates a part of the final thresholding showing water surfaces as shaded blue area.

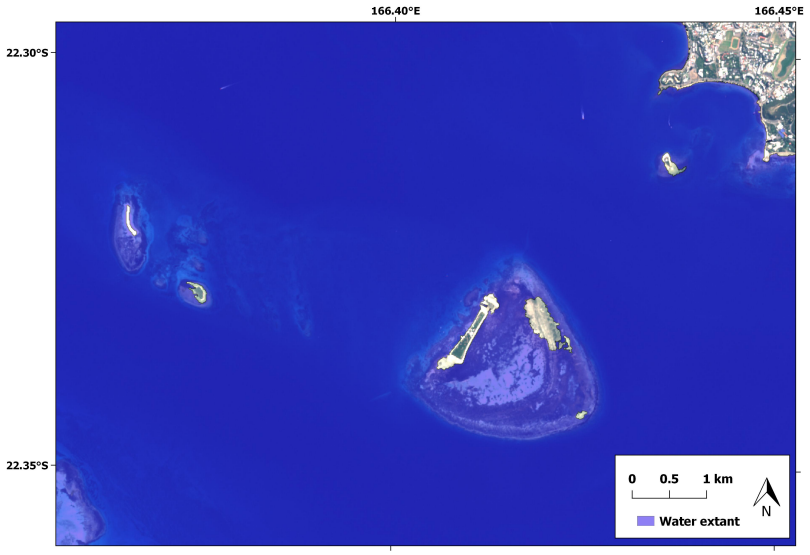


**Figure 8:** Soil thresholding: pixels selected as water surfaces are displayed in blue

### 2.4.2 Sun Glint Removal

As explained in the section 2.2, an image produced by Sentinel-2 is the result of 12 different detectors. Consequently, slight differences in the geometries of the settings of each detector produce disparities between their footprints. Indeed, as the geometrical settings of the detectors are different, the specular reflection on their footprints is also different. Above land, most of the reflection is diffuse which makes these disparities insignificant. Above water, the disparities are clearly visible and have to be corrected.

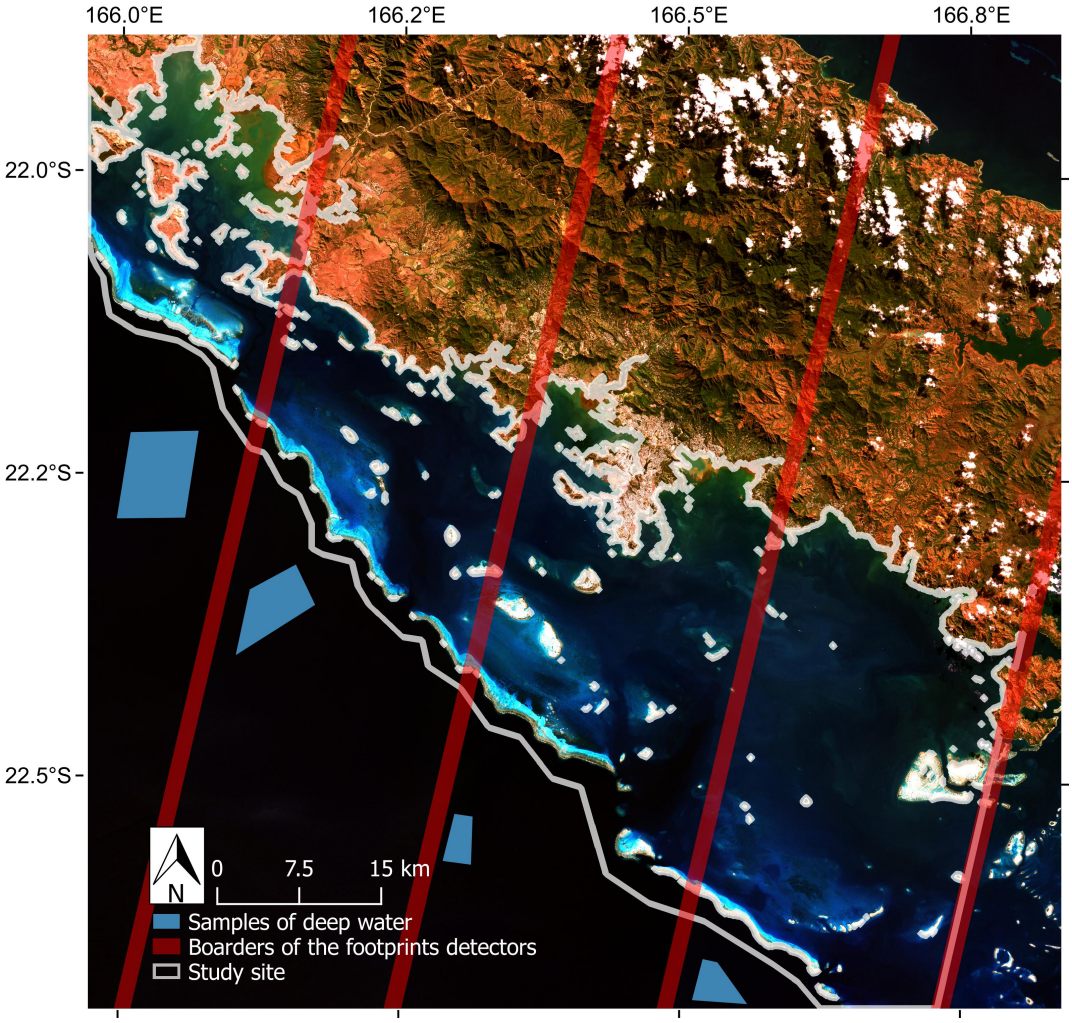


**Figure 9:** Localization of samples of deep water and boarders footprints of the detectors in the study site

In this context, the method proposed by Hedley et al. [2005] has been applied. It requires the selection of a sample area in which the underwater brightness is considered as homogeneous but with evident variation of the sun glint. Figure 9 shows the localization of these samples. The samples have to be large enough to contain the overall variation of sun glint. Du to the homogeneous underwater brightness, they are, most of the time, selected above deep area. However, homogeneous water optical properties are also recommended. For this reason, samples have differ-

ent sizes, due to the need to avoid the selection of visible disparities potentially induced by water flows coming from the passes with different optical properties. As shown by its spectral signature, the diffuse reflectance of the water on the near-infrared domain is insignificant. It is then possible to assume a good description of specular reflection with the variation of the near-infrared signal. The method consists in establishing the linear regression of a near-infrared against a visible band. The correction process is computed as follows :

- $R'_i$, The corrected value of the pixel in the visible band $i$
- $R_i$, The initial value of the pixel in the visible band $i$
- $b_i$, The slope of regression of NIR band against the visible band $i$
- $R_{NIR}$, The value of the pixel in the NIR band
- $Min_{NIR}$, The minimum value observed among every pixels contained in the sample, in NIR band

$$\boxed{R'_i = R_i - b_i(R_{NIR} - Min_{NIR})} \tag{3}$$

The value of the pixel which has to be corrected in band i is reduced by the product of the regression slope and the difference between its NIR value and the sample minimum NIR value.

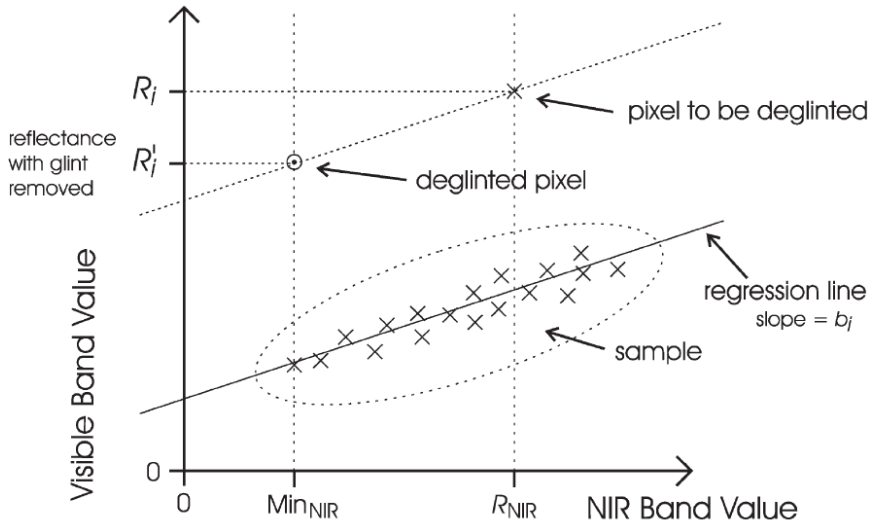


**Figure 10:** Sun glint removal process (figure taken from Hedley et al. [2005])

## 2.5 Bottom type and water classification

As seen in section 1.3, the water surface reflectance is dependent on the bottom type reflectance and on the attenuation process along the pathway downward and upward of the radiation. This attenuation is itself dependent on the water compounds, leading to differences in optical properties. The attenuation is also dependent on the depth which reduces or increases the pathway. As shown in literature, it can be useful to suppress or reduce the variation due to the bottom type reflectance and water quality from the radiation signal measured by the satellite. Minghelli-Roman and Dupouy [2014] proposes to suppress effect of water attenuation from the signal to retrieve bottom reflectance. Literature also proposes to classify the bottom type on the basis of descriptors decorrelated from depth variation [Manuputty et al., 2017, Manessa et al., 2014, Manuputty et al., 2015] . In this work, a classification approach is evaluated as initial step. It aims at creating sub-datasets of observations in order to isolate the part of their variation driven by depth from those driven by bottom reflectances and water optical properties. The dataset describes pixels as observations with the descriptors illustrated in the following section.

### 2.5.1 Descriptors : Depth Invariant Index

In 1980, Lyzenga described a method allowing to create an optical index invariant from depth variation. As shown in section 1.3, the measured radiance responds exponentially to the depth variation. Conversely, the response is a linear function of the reflectance. Thus, by comparing the log radiance of two signals on different wavelengths above a uniform bottom type, it is possible to infer the linear trend describing the attenuation variation along the depth of a water-column. In case of homogeneous water optical properties and bottom types, the log radiances are set on a linear trend. Its slope corresponds to the ratio of the attenuation coefficients of the two wavelengths [Philpot, 1989]. In case of homogeneous water compounds and two different bottom types, the log radiances are set on two linear trends with the same orientation but different intercept. The shift which is due to the intercept is directly induced by the variation of reflectance of the bottom types. However, if the water optical properties are heterogeneous, the attenuation coefficients k become variable and the observation does not lie on a straight line. Figure 15 shows the plot of two different samples taken on different locations on the study site. The Depth Invariant Index (DII) is directly linked to the shift between the linear trends.
The following equations 4-8, applied on a sample of pixels describing a homogeneous bottom type, allow to compute the ratio of attenuation coefficients :

- $R_i$, The initial radiance value of the pixel in the visible band $i$
- $R_{deep,i}$, The average radiance value in the visible band $i$ of a sample of pixels selected above deep water
- $k_i$, The water attenuation coefficient of the visible band $i$
- $Min_{NIR}$, The minimum value observed among every pixels contained in the sample, in NIR band
- $d_{ij}$, The invariant depth index or the shift of the trend corresponding to a bottom reflectance

$$X_i = ln(R_i - R_{deep,i}) \tag{4}$$

**Table 4:** Inventory of the Combination used for the computation of DII

| | | | i | | | | |
|---|---|---|---|---|---|---|---|
| | Band | number | 1 | 2 | 3 | 4 | 5 |
| j | Shorter Blue | 1 | | ✓ | ✓ | ✓ | ✓ |
| | Blue | 2 | | | ✓ | ✓ | ✓ |
| | Green | 3 | | | | ✓ | ✓ |
| | Red | 4 | | | | | ✓ |
| | Longer Red | 5 | | | | | |

$$X_i = \frac{k_i}{k_j} X_j + d_{ij} \tag{5}$$

$$\frac{k_i}{k_j} = a + \sqrt{a^2 + 1} \tag{6}$$

$$a = \frac{\sigma_{ii} - \sigma_{jj}}{2\sigma_{ij}} \tag{7}$$

$$\sigma_{ij} = \bar{X_i X_j} - (\bar{X}_i \bar{X}_j) \tag{8}$$

Equation 4 allows to linearize radiance data, whereas the subtraction of the deep water signal removes the scattered radiance. Here, scattered radiance refers to the part of the incoming radiation which never reaches the bottom and is sent back toward the atmosphere due to volume scattering. The process allows to defined $\frac{k_i}{k_j}$ on the basis of a sample with consistent bottom type. Then, the invariant depth index can be estimated on the total area by the following equation :

$$\boxed{d_{ij} = X_i - \frac{k_i}{k_j} X_j} \tag{9}$$

The method acts as a rotation of $arctan(\frac{k_i}{k_j})$. In this study, with unsure bottom type, the correlation between the blue and green band can be taken as an indicator of uniformity over the sample [Philpot, 1989]. The method made the assumption of uniform water compounds over the study site. Table 4 shows the bands' combination used for the computation of DII. Classification is then using 10 depth invariant index as descriptors.

### 2.5.2 Descriptors: Hue

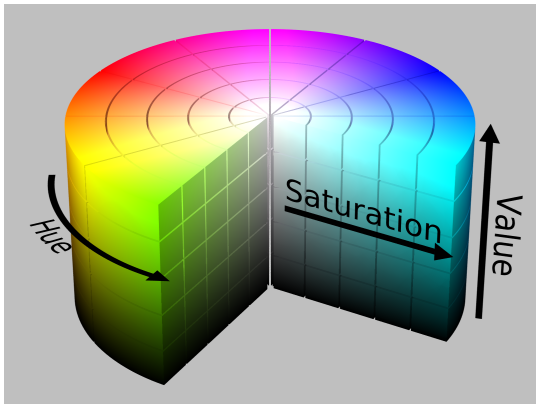


**Figure 11:** Representation of the HSV space as a cylinder (figure taken from wikipedia)

In order to extract a last descriptor, the position of every pixel is transformed from a RGB space, with bands 4,3,2 as red, green and blue, to a HSV space. HSV space is commonly used for image classification [Maheswary and Srivastava, 2009]. It is described by 3 values : the Hue, the Saturation and the Value. Figure 11 shows a visualization of this space. The Hue value of a pixel describes its pure color and is invariant from its gray level. The Value describes its own brightness and the Saturation is a measure of Chrominance relative to the brightness. The conversion is computed as follows:

$$Cmax = max(R, G, B) \tag{10}$$

$$Cmin = min(R, G, B) \tag{11}$$

$$C = Cmax - Cmin \tag{12}$$

$$H = Cmax - Cmin \tag{13}$$

$$\boxed{H = \begin{cases} 0°, if C = 0 \\ 60°(\frac{G-B}{C} mod 6), if Cmax = R \\ 60°(\frac{B-R}{C} + 2), if Cmax = G \\ 60°(\frac{R-G}{C} + 4), if Cmax = B \end{cases}} \tag{14}$$

$$S = \begin{cases} 0, if Cmax = 0 \\ \frac{C}{Cmax}, if Cmax \neq 0 \end{cases} \tag{15}$$

$$V = Cmax \tag{16}$$

- $R, G, B$ The Red, Green and Blue values on the range [0:1]
- $C$, The Chrominance on the range [0:1]
- $S$, The Saturation on the range [0:1]
- $V$, The Value on the range [0:1]
- $H$, The Value on the range [0:360] degrees

As the Value and the Saturation are strongly influenced by the attenuation of the signal, the Hue should remain more stable relative to the bottom reflectance in shallow depth.

### 2.5.3 Classification process: K-means

In this project, classifications processes have been achieved using the scikit-learn package of python [Buitinck et al., 2013]. K-means algorithm is one of the most popular methods for the classification of pixels [Dhanachandra et al., 2015]. It allows an unsupervised classification achieved on the basis of the positions of observations in the descriptors space. The spatial settings of the observations, in our case georeferenced pixels, are not taken into account [Fua, 2018]. The purpose of the algorithm is to classify a number of observations in a specified number of clusters, k , minimizing the inertia or the within-cluster sum-of-squares, described by equation 17. The within-clusters inertia is relative to the euclidean distance between observations and their clusters.

$$I(c, \mu) = \sum_{i=0}^{N} \left\| x^i - \mu_{c^i} \right\|^2 \tag{17}$$

- $c$, The assignment parameter which attributes to each observation a cluster
- $\mu$, the centroid position of a cluster in the descriptor space
- $x$, The observation or pixel in the descriptor space : $x^i \in \mathbb{R}^d$
- $N$, The number of observation

The resolution method is composed of 3 steps : an initialization followed by two iterative steps allowing the convergence [Andrew, 2015]:

1. Initialize K cluster centroids $\mu_1, \mu_2, ...\mu_K \in \mathbb{R}^d$
2. Iterate until convergence:
   - Assign to every observation the cluster with the closest centroid: $c^i := \underset{k}{argmin} \left\| x^i - \mu_k \right\|^2$ (18)
   - Update to every cluster its centroid position : $\mu_k := \frac{\sum_{i=0}^{N} \{c^i == k\} x^i}{\sum_{i=0}^{N} \{c^i == k\}}$ (19)

As a result, the first iterative step (18) minimizes the inertia, $I(c, \mu)$ with respect to $c$ whereas the second (19) minimizes it with respect to $\mu$. In this study, a classification model is produced by the best Inertia among ten different runs.

**Standardization:** In order to ensure comparable scales of distance on every dimension of the descriptor space, K-means algorithm requires a standardization of the dataset.

- $\bar{x}_d$, the average value of the descriptor $d$ : $\bar{x}_d = \frac{\sum_i^N x_{i,d}}{N}$ (20)
- $s_j$, the deviation value of the descriptor $d$ : $s_d = \sqrt{\frac{1}{N} \sum_i^N (x_{i,d} - \bar{x}_d)^2}$ (21)
- $z_{i,d}$, the standardized value of the observation $i$ for descriptor $d$

$$z_{i,d} = \frac{x_{i,d} - \bar{x}_d}{s_d} \tag{22}$$

The resulting descriptors' values are centered around 0 and their range [-1:1] describes their standard deviation.

It has to be precised that classifications are fitted without pixels belonging to detectors' footprint boarders, as visible on Figure 9. Indeed these pixels, in-between 2 distinct detectors' footprint, clearly show disparities on Sentinel-2 images. Whereas pixels produced by a unique detector become homogeneous among footprints, as glints are removed, the disparity on the footprint boarders remains. Such pixels are removed from every fitting, selection or validation process of the present work.

## 2.6 The number of clusters

Choosing a suitable number of clusters during unsupervised classification is always a delicate task. As one of the research question of this study is to propose and evaluate a method with a classification as initial step, two options are tested. In a first option, a restricted number of clusters is chosen in order to achieve a classification describing only a small amount of the information contained in the dataset. In this case, the dataset is only clustered by its primary dissimilarities. In a second option, a high number of clusters is chosen which allows a classification describing a large amount of information. The dataset is clustered until clusters become too much similar.

To this end, two complementary analyses are carried out. The first one relies on the agglomerative hierarchical clustering based on Ward's method and is aimed to aggregate observations following their dissimilarities. The second analysis, based on the silhouette index, is evaluating how well an observation is assigned to its cluster.

### 2.6.1 Agglomerative hierarchical clustering

Agglomerative hierarchical clustering is described as an ascendant method. It clusters the observations following their similarities until only one global cluster is obtained. The dissimilarities are measured by a distance established between each observation and cluster in the descriptor space. Several distances can be used. In this study the Ward's method is used which imposes a specific distance. The analysis relying on agglomerative hierarchical clustering have been achieved using the FactoMine package of Rstudio [Lê et al., 2008].

The global process is the following one [Tibshirani, 2009]:

1. Start with each observation as a cluster.
2. Until only one cluster remains:
   (a) Find the closest pair of clusters.
   (b) Merge them.

**Ward's method:** Ward's method, like K-means algorithm, relies on the concept of Inertia. As seen in section 2.5.3, the inertia is a measure of variances. However, three different measures can be achieved on a clustered dataset: the total inertia, the within-clusters inertia and the without-clusters inertia. Following the theorem of Huygens [Wikipedia, 2015], total inertia is equal to the addition of the within-cluster inertia and without-clusters inertia:

$$\sum_{c=0}^{K}\sum_{i=0}^{N}\left\|x_c^i-\bar{x}\right\|^2=\sum_{c=0}^{K}\sum_{i=0}^{N}\left\|x_c^i-\mu_{c^i}\right\|^2+\sum_{c=0}^{K}\sum_{i=0}^{N}\left\|\mu_{c^i}-\bar{x}\right\|^2 \tag{23}$$

Ward's method aims at minimizing the within-clusters inertia and therefore maximizing the without-clusters inertia. The agglomeration of two clusters necessarily increase the within-clusters inertia or decrease the without-clusters inertia. Ward has shown that this increase of within-cluster inertia is equal to:

$$\delta(A,B)=\sum_{i\in A\cup B}\left\|x_{A,b}^i-\mu_{A\cup B}\right\|^2-\sum_{i\in A}\left\|x_A^i-\mu_A\right\|^2-\sum_{i\in B}\left\|x_B^i-\mu_B\right\|^2=\frac{n_A n_B}{n_A+n_B}\left\|\mu_A-\mu_B\right\|^2 \tag{24}$$

Taking this formulation (24) as measure of distance allows to aggregate clusters following the increase of variance caused by their merging [Tibshirani, 2009, Murtagh and Legendre, 2014].
In this study, agglomerative clustering following Ward's method is achieved on random subset of the dataset. It allows a clustering based on the same concept as for the k-means, Inertia, and to evaluate the maximum number of division allowing a significant change in inertia.

### 2.6.2 Silhouette index

The second analysis relies on the silhouette index. It aims at estimating how similar is an observation to its cluster. The index ranges from -1 to 1 and is computed as follows :

$$s(i)=\frac{b(i)-a(i)}{max(b(i),a(i))} \tag{25}$$

- s(i), The silhouette score for the observation i
- a(i), The average distance between the observation i and the observations of its cluster
- b(i), The lowest average distance between the observation i and the observation of one of the other cluster.

An index close to 1 highlights an observation fully similar to its cluster and well separated from the other cluster. On the opposite an index close to -1 shows an observation which would fit better in a neighboring cluster. As the index is close to zero, the observation lie on the border of two clusters [Rousseeuw, 1987].
This analysis is processed on two randomly selected sub-datasets, classified by K-means method from 2 to 14 clusters.

## 2.7 Empirical modeling

### 2.7.1 Lyzenga

From equation (2), Lyzenga [1978] proposed to reduce error due to variation of bottom reflectances and water optical properties by a linear combination of several spectral bands. He defined a depth algorithm of the form :

$$\hat{z} = h_0 - \sum_{j=1}^{N} h_j \ln(L_j - L_{sj}) \tag{26}$$

- $\hat{z}$, The estimated depth
- $N$, The number of spectral bands
- $L_j$ The corrected radiance (from sun glint and atmospheric effect) as observed on the band $j$ at satellite location
- $L_{sj}$ The average deep water radiance after correction
- $h_0$, An offset parameter
- $h_j$, N parameters of regression corresponding to each spectral band.

Inconveniently, this method relies on the subtraction of the average deep water signal $L_{sj}$, in order to get rid of the volume scattering. It can lead to negative log above area with low bottom albedo, such as seagrass, making the depth prediction impossible [Stumpf et al., 2003].

Assumptions of relatively stable water optical properties on the image extent has to be made. In theory, bathymetry up to 25 meters can be evaluated thanks to the blue band penetration property. Besides, obtained depths are theoretically insensitive to a certain range of variation of the water-attenuation coefficients and of bottom reflectances, thanks to the use of several spectral bands as a linear combination [Lyzenga et al., 2006]. In practice, stability of the results is still influenced by variations of environmental parameters such as turbidity and heterogeneous benthic substrates [Stumpf et al., 2003, Philpot, 1989, Hengel and Spitzer, 1991].

Table 1, shows a high range of variation of the maximal predictable depth by this method among the different case studies. With this in mind, it is possible to suppose different maximum predictable depth between class of bottom type. In this study the maximum depth is taken as a parameter for filtering the in-situ measurements used for the models training. The variation of predictable depth among classes is studied by the selection of models following their performances.

### 2.7.2 Stumpf

Stumpf et al. [2003] observed that having to empirically adjust five parameters (in case of two bands used: $L_{s1}$, $L_{s2}$, $h_0$, $h_1$, $h_2$) tend to make Lyzenga's algorithm unstable for large areas, even in small water quality variation conditions. He developed an alternative method based on the ratio of the signal recorded in two different wavelengths.

$$\boxed{\hat{z} = m_1 \frac{\ln(nL_w(\lambda_i))}{\ln(nL_w(\lambda_j))} - m_0} \tag{27}$$

- $Z$, The water depth
- $L_w$, The water radiance
- $\lambda_i$, The spectral wavelength i
- $n$, A fixed constant for all areas allowing to assure positive logarithm and linear response with depth
- $m_0$, $m_1$, Two minimizing parameters : offset $m_0$, and coefficient $m_1$

Mapping shallow bottom resulting in a negative difference of radiances ($(L_j - L_{sj}) < 0)$) with respect to deep water is therefore possible with fewer empirical parameters. Relationship with depth relies no more on a simple logarithm but on a ratio between logarithms of spectral bands. In this case, an increase in depth induces a larger decrease of the radiance which has the largest wavelength. Indeed, a green band, for example, undergoes a higher absorption than blue bands and have a higher rate of decrease of its logarithmic radiance with depth. Comparatively, a change in bottom type affects all bands similarly. In other words ratio undergoes much greater changes with depth than with bottom variation [Philpot, 1989]. Stumpf's method is therefore more stable to heterogeneous benthic substrates.

As a weakness, Stumpf method produces a slight increase in noise. In case of too low ground resolution, depth predicting performance decreases [Stumpf et al., 2003].

## 2.8 Selection and validation of the models

In this study the maximum depth is taken as a parameter for filtering the in-situ measurements used for the models training. Furthermore a maximum depth variance of pixels having several in-situ measurements, is also taken as a parameter for filtering the training dataset. The purpose of this filter is to get rid of detectable pixels with is highly irregular depth. Indeed, the measurement of depth in a 100 $m^2$ area is likely not to be representative from the average depth of the area. The variation of maximum predictable depth and variance depth among classes is studied by the selection of models following their performances.

### 2.8.1 Bias–variance trade-off

The main issue during predictive models fitting is the generalization error. This error is defined by the false predictions expected on new data, independent of the training dataset, used to fit the model [Murphy, 2012].

Two components allow a description of this error [Andrew, 2015]. A first component called bias, describes a too simple model or a model having not enough parameters. Such a model, even if fitted to a large number of observations will always fail to precisely translate the phenomenon we want to predict. A second component is defined by the variation of the fitting process. A high variation is observed between several fittings of too complex models or typically models fitted with too many parameters regarding the size of the dataset. In this case, models resulting from the fitting highly variate according to the training dataset. Indeed, random aspect of the dataset, independent of the studied phenomenon, will be modeled.

In others words, simple models tend to fit only essential aspects of training datasets. In this case, even if trained with small datasets, such models applied on new data will bring similar predictions. The fitting process has only little variation because the learned aspects are globally the same among the models. However, a large bias occurs on these models because they are not able to describe all the aspects of the studied phenomenon. On the contrary, complex models, or models with too large number of parameters, bring the risk to model aspects which are particular to their training dataset. Strong differences will result from these models once used to predict new data, slightly different from their training dataset. These models have a strong variation and are said to be over-fitted.

### 2.8.2 Stratified K-folds

The tests of different parameters setting aims at selecting the fitting process with the optimal bias-variance trade-off. To this end, it is required to divided the dataset into training and testing dataset. The generalization error is then evaluated on the testing dataset.

In this work, resulting models are selected and validated using the K-folds method. During each fitting, the dataset is divided into 4 folds. The model is trained 4 times on a set of 3 filtered folds and tested 4 times, each on the last remaining unfiltered fold. Each fold is keeping the stratification of the original dataset. As an example, a depth-predictive model aimed at predicting a 2000 pixels

class, resulting from the bottom type classification, is divided into 4 trainings of 1500 pixels and 4 testing datasets of 500 pixels. In each of the dataset the stratification of the original 2000 dataset is kept.

# 3 Results

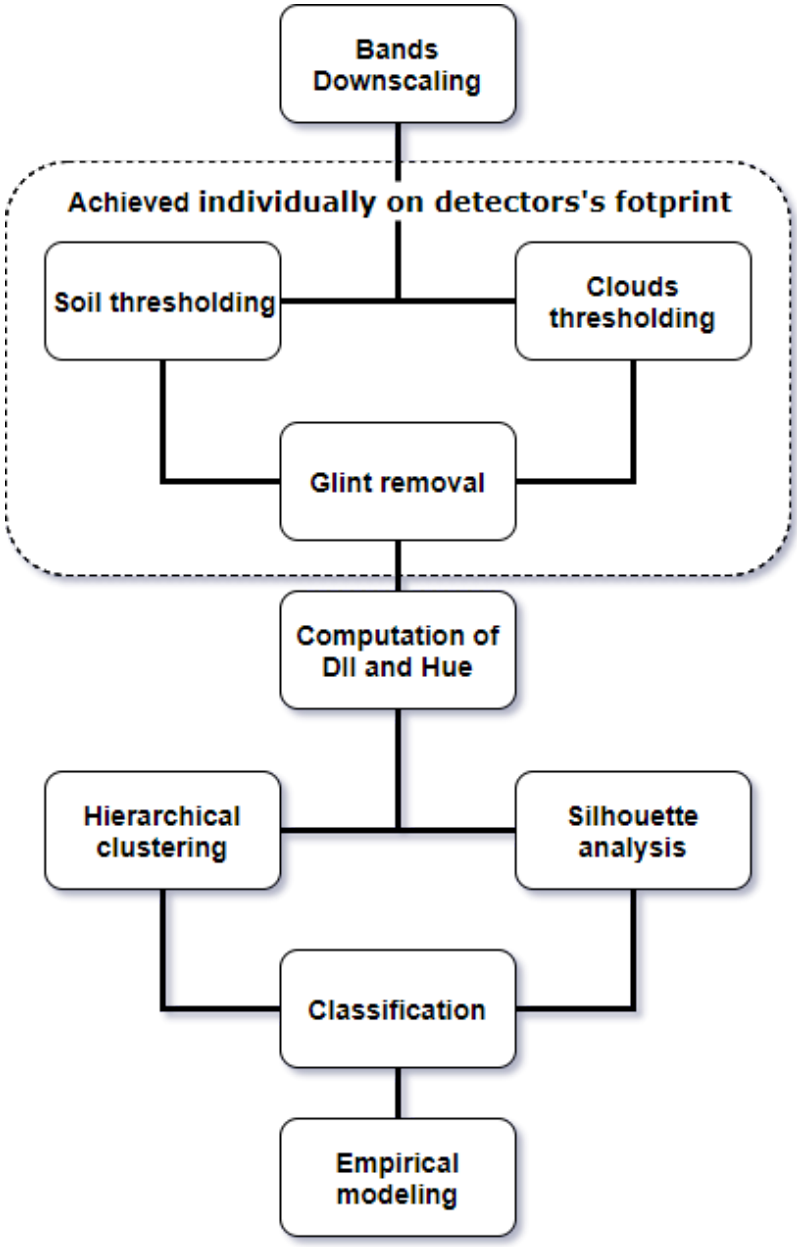


**Figure 12:** Workflow of the proposed methodology

Figure 12, sum up the proposed methodology. As a first step, Bands 1, 9, 5 and 8a are downscaled in order to reach a ground resolution of 10 meters. Soil and clouds are thresholded individually on the detectors' footprint. Sun glint is then removed individually also. Depth invariant index and Hue are computed as descriptors for the classification. Two different analysis, aims at defining numbers of clusters for high and low level classification, are achieved. Unsupervised classification is achieved. Finally empirical model are fitted individually on classes.

## 3.1 Sun glint removal

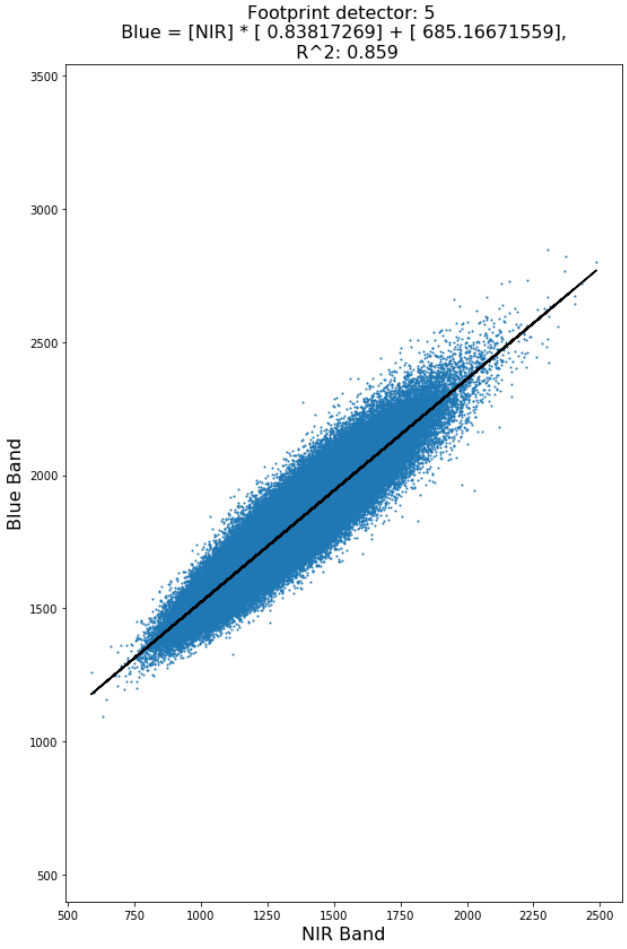


**Figure 13:** Regression of Blue band on the NIR band for Footprint detector 5

Figure 13, shows an example of regression of the NIR band 8 on the blue band 3, computed on the sample of one of the detectors' footprint. The evident correlation between the two signals enforces the assumption of specular reflection as a main factor of variation of the radiation.

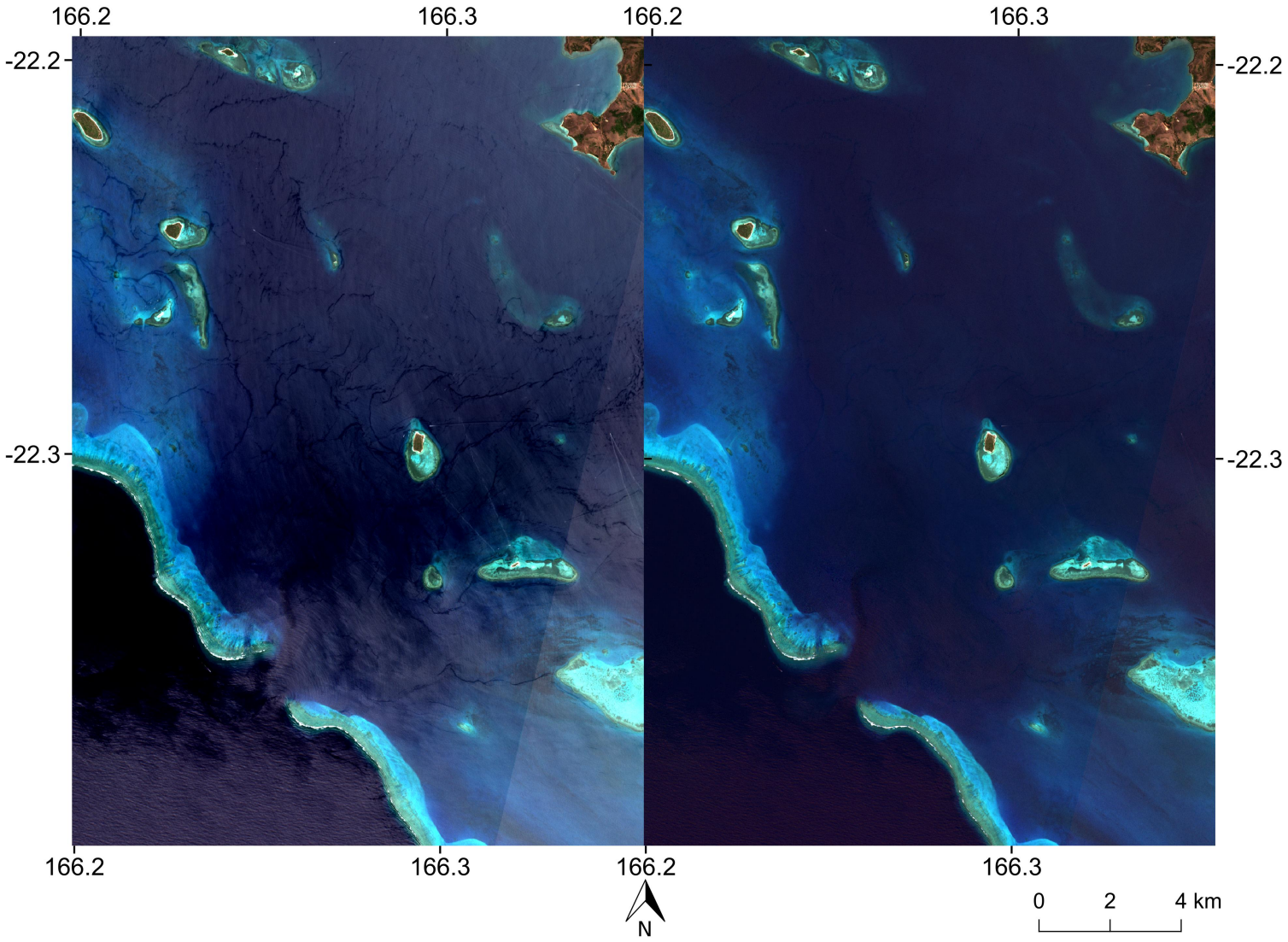


**Figure 14:** Comparison of a parcel of image before (on the left) and after (on the right) the glint removal processing. Both images have the same range of colors sampling

Figure 14, illustrates the results of the glint removal processing above a channel area displaying heterogeneous glints. The original image, shows some clear irregular patterns on the water surface. These patterns are due to water flows through the passe. In addition, the difference in glint intensity between the two detectors' footprint appears as a linear disparity. The result of the glint removal process shows a clean water surface without any irregular patterns. The disparity, induced by the difference of the geometrical setting between detectors is also strongly reduced.

## 3.2 Computation of the descriptors

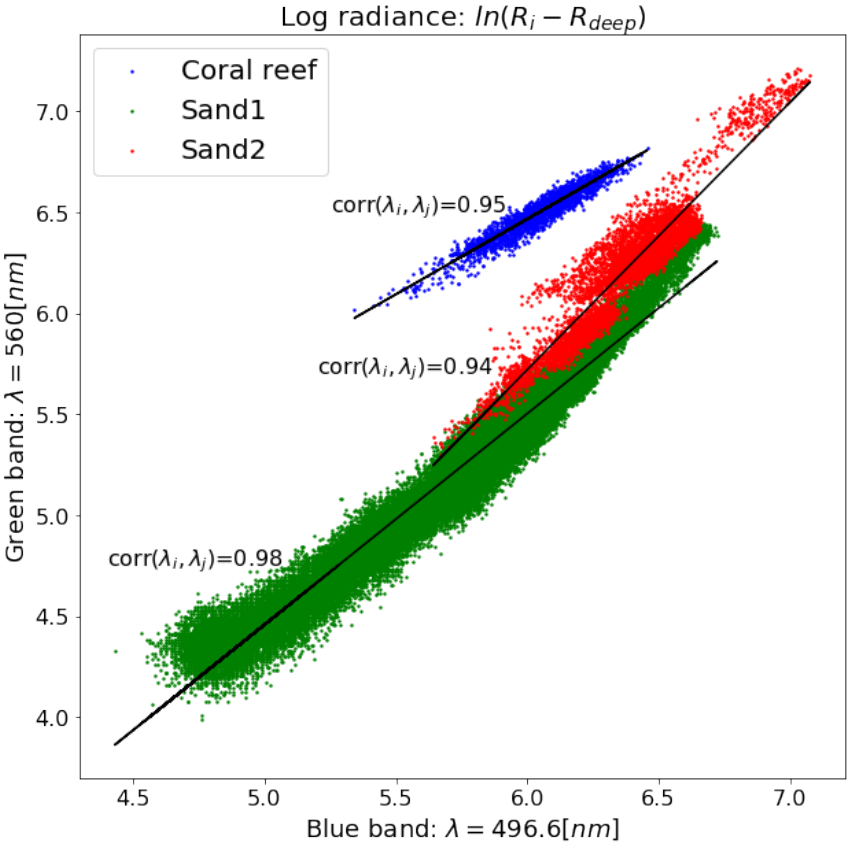


**Figure 15:** Three samples of log radiances with different and homogeneous bottom types. The sampled coral reef lies on the northern part of the study site whereas the sandy sample lies on central detector's footprint. The second sand sample, scattered in red lies on the South part of the study site and is not homogeneous

Several examples of samples, aim at selecting homogeneous bottom substrate, and extracted on different location of the study site, are displayed in Figure 15. Two samples are assumed to represent sandy bottom and one is assumed to display coral reef extent. Figure 16 give the localization of the extracted samples. The sandy sample, scattered in red, has an irregular distribution on a slightly different slope and a lower correlation. It can be supposed that it represents heterogeneous substrates. Samples scattered in blue and green show close slopes despite their different locations. Consequently, the water optical properties could be assumed to not vary a lot from the north part of the studied site to the central part of it. The sample with the highest correlation is kept for the computation of DII.

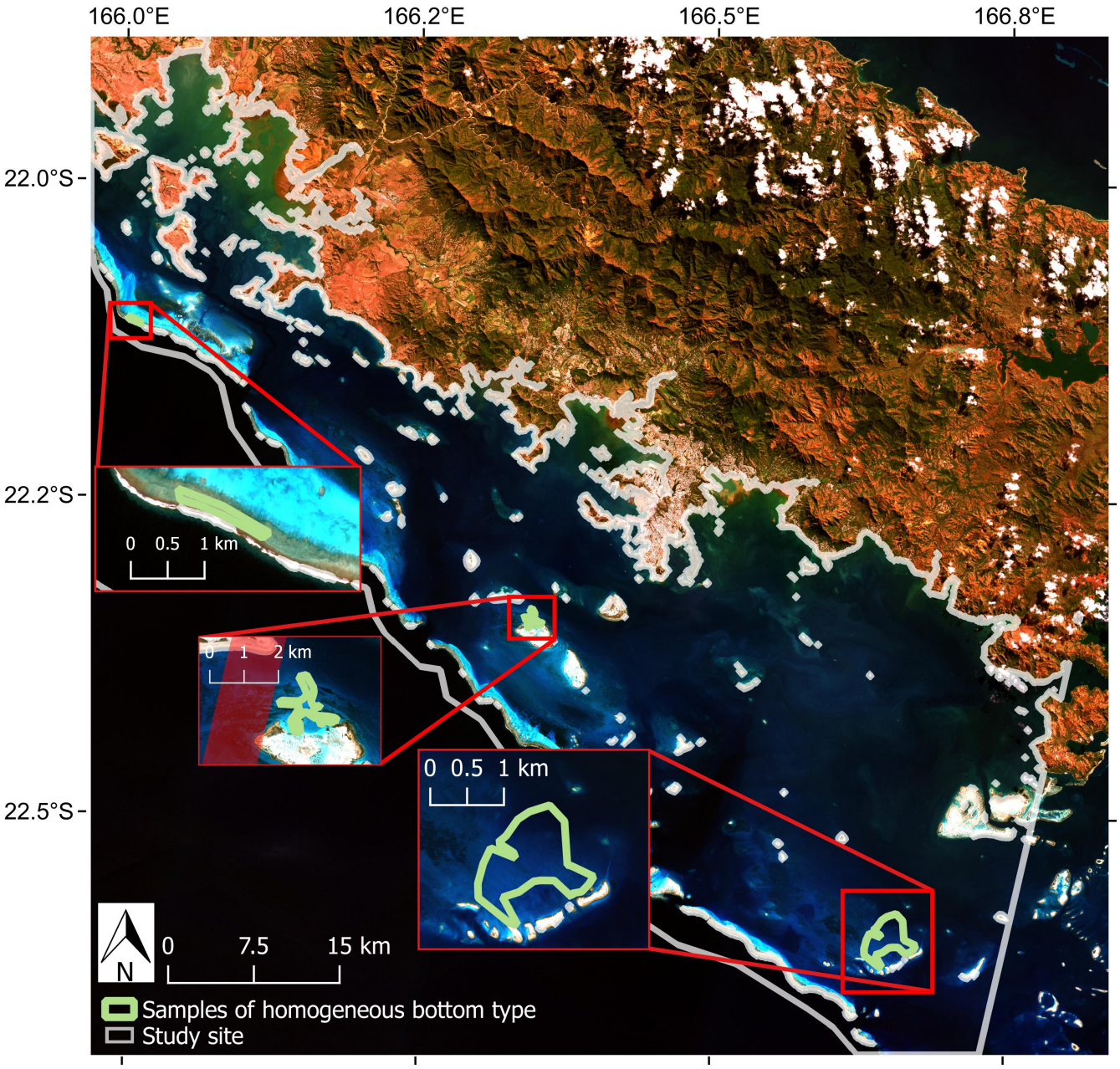


**Figure 16:** Localization of samples of homogeneous bottom type in the study site

Figure 17, illustrates the classification process. Descriptors Hue and DII produced by the combination of Green and Blue band (bands 2 and 3) are visible with the resulting of an eight-clusters classification and the initial RGB image. Due to its high brightness, the extent on the back of the barrier reef can be assumed to be a sandy bottom substrate. On the RGB image, this extant shows some patterns which are strongly attenuated on the DII map. Hue map also shows a slighter attenuation of these patterns. Consequently, these patterns should be supposed to be driven by depth variation and are not visible on the resulting classification.

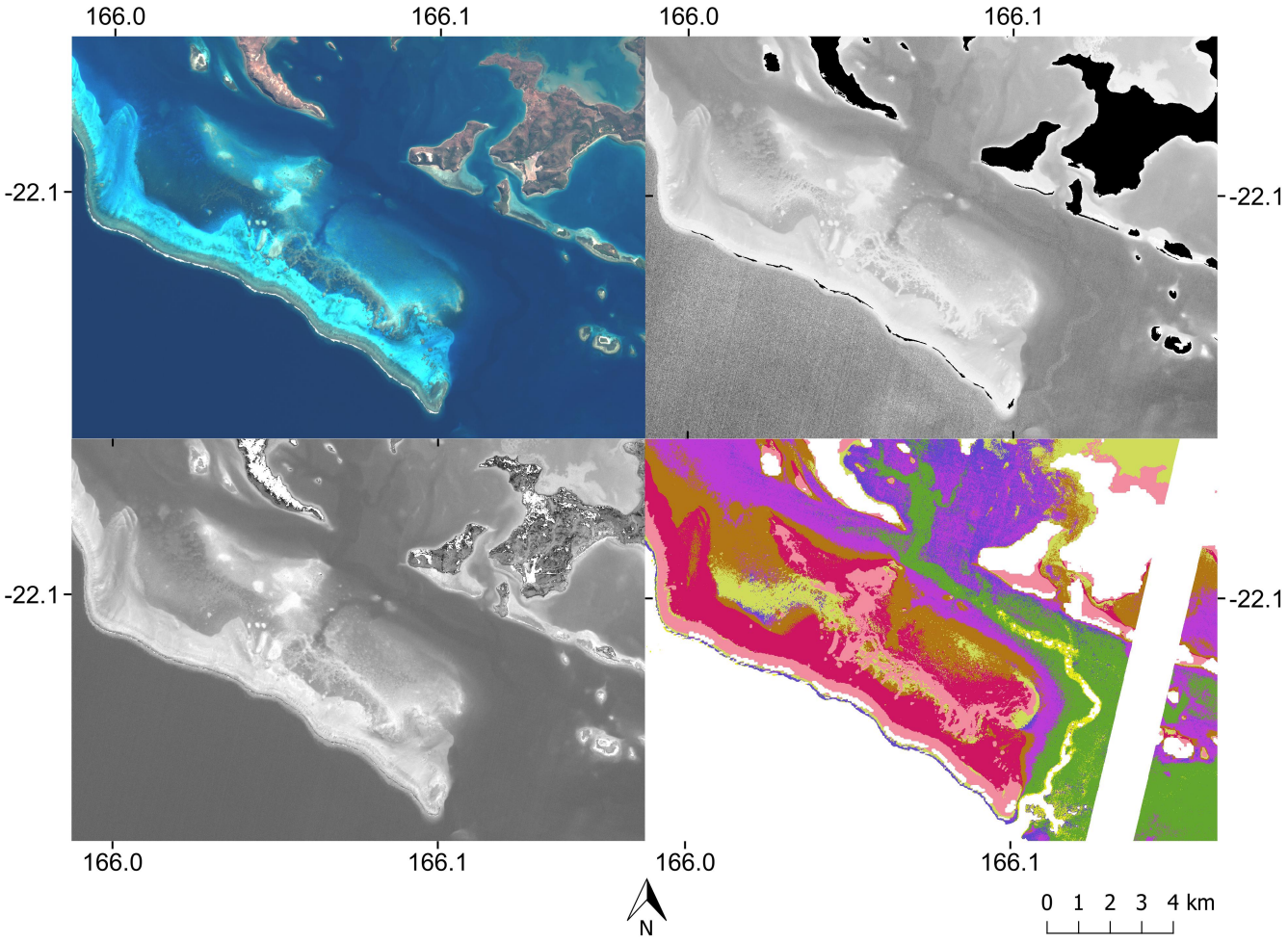


**Figure 17:** Comparison between glint-free RGB image(upper left), the DII from Green and Blue bands (upper right), the Hue (lower left) and the resulting classification (lower right)

## 3.3 Agglomerative hierarchical clustering

Figure 18 shows the loss of within-clusters inertia as the number of clusters increases in the agglomerative hierarchical clustering applied with Ward's method. The analysis is achieved on 4 different samples, randomly selected with different sizes. The figure shows stable results among the 4 samples. Only a number of 3 clusters allows a large loss of within-cluster inertia. Therefore a number of 3 clusters is chosen as restricted option for the classification describing only a small amount of the informations contained in the dataset.

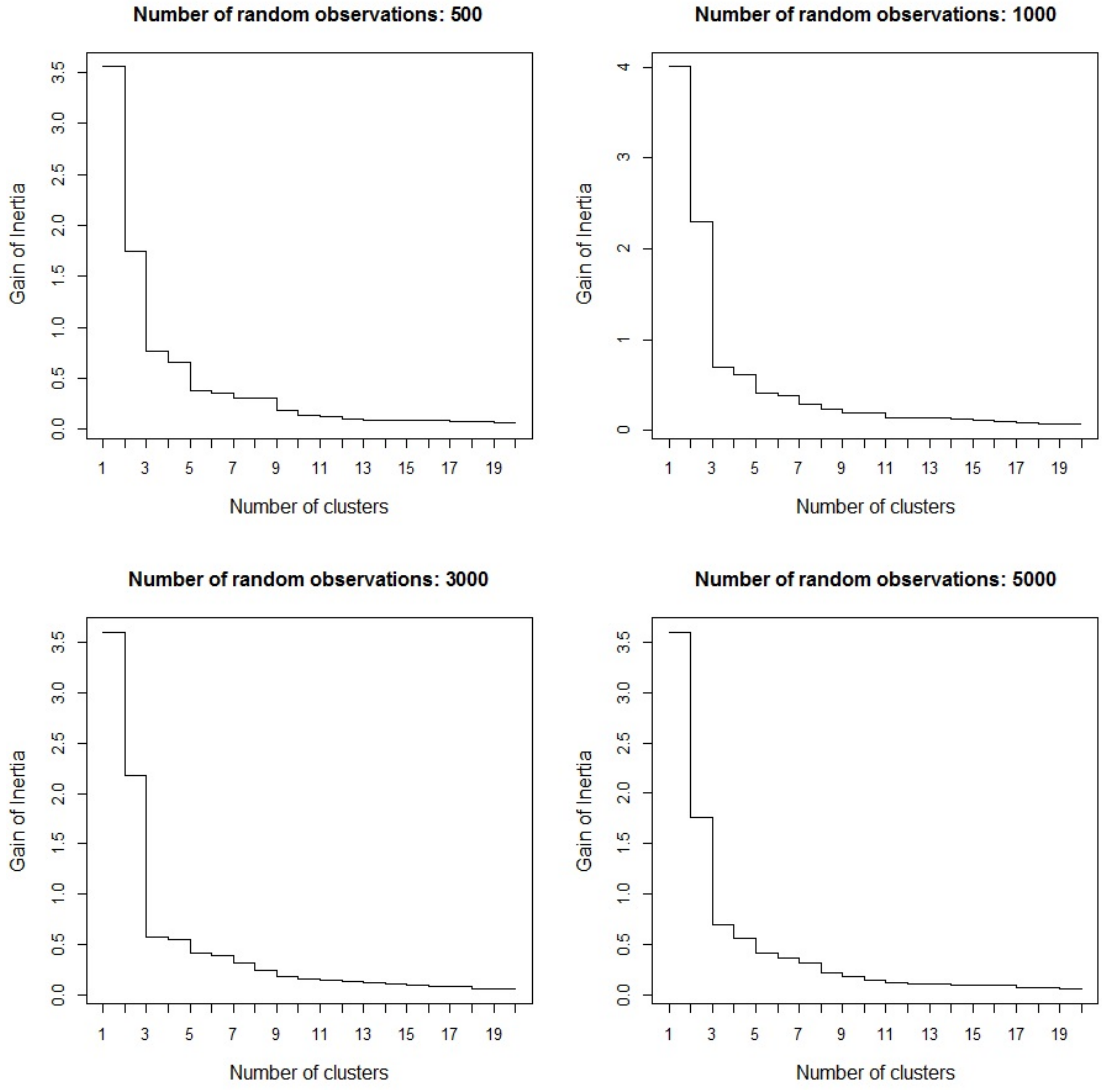


**Figure 18:** Loss of within-cluster inertia as an additional cluster is created

## 3.4 Silhouette index analysis

The results of the silhouette indices are visible on Figures 32 - 35 , in the Annex of this report. Figure 19, shows the evolution and the gain of the average silhouette index resulting from each K-means classification as the number of clusters increases. It is clear that increasing the number of clusters reduces the average silhouette score, due to the proximity of the majority of the observations in the descriptor space. However, some specific number of clusters produce systematic poor or slightly better clustering. As shown by Figure 19, a number of 7 clusters is critical whereas a slight gain occurs on each dataset, as the number of clusters pass from 5 to 6 and from 7 to 8. The number of 8 clusters is then kept as the option for high number of clusters.

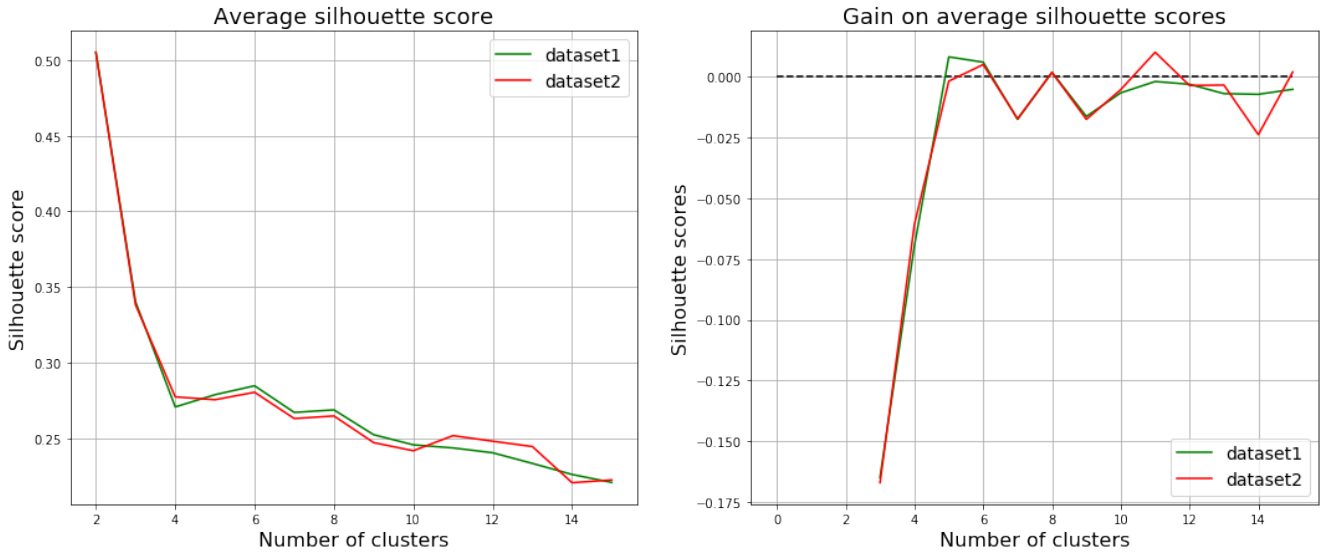


**Figure 19:** Evolution of average silhouette scores (left), gain on average silhouettes scores (right)

## 3.5 Classification

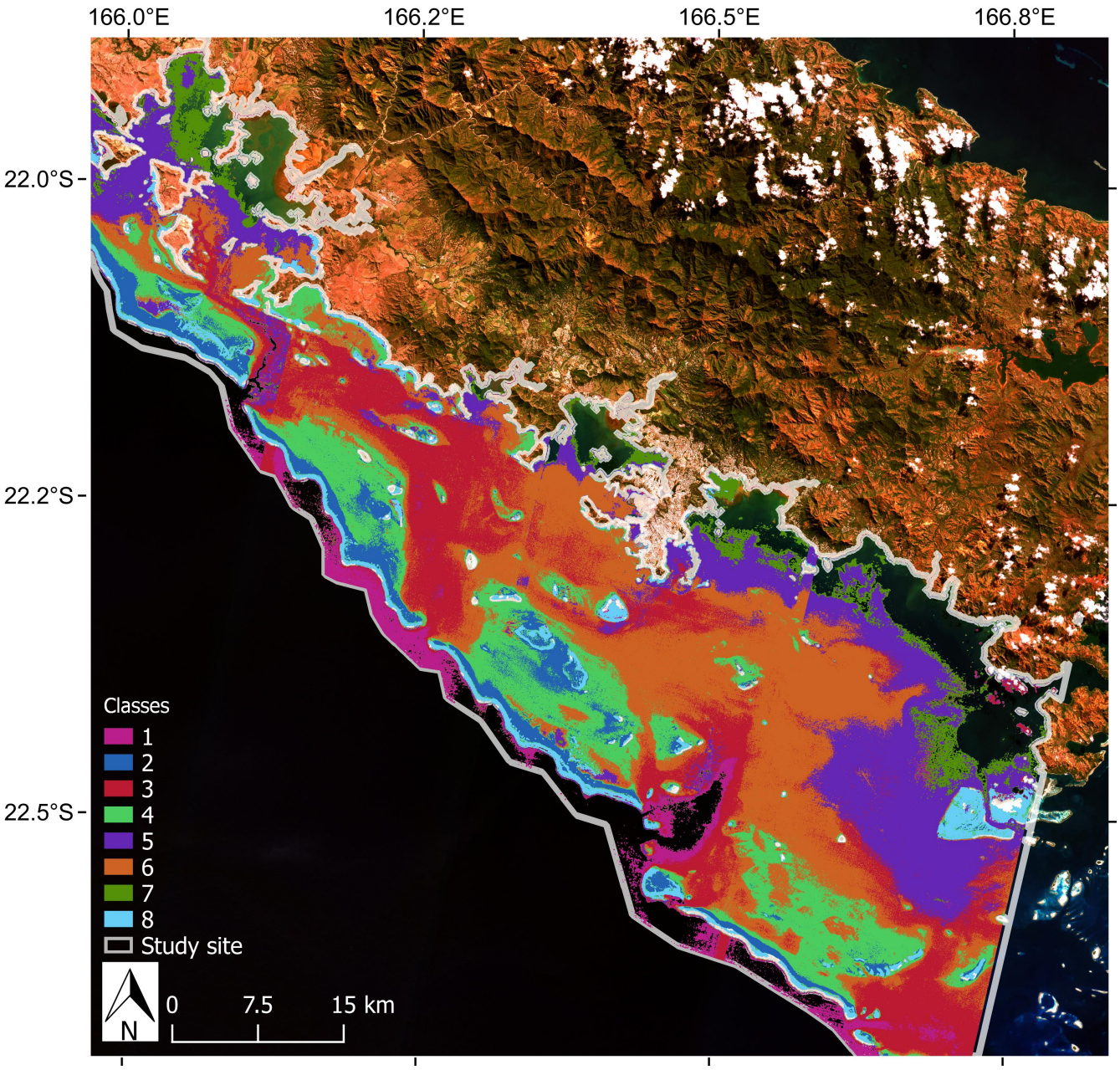


**Figure 20:** Classification in 8 clusters following bottom reflectances and water properties

Figure 20 shows the resulting 8 classes classification following DII and Hue over the study site. As explained in section 2.5.3, the pixels located in-between 2 distinct detectors' footprint does not take part of the classification's fitting process. Missing values of those in-between pixels are fulfilled in Figure 20 by a prediction using the k-means model, fitted on pixels belonging to a unique footprint. Some linear patterns, mainly on class 3, are visible on the footprints' boarders. Despite this, the classifications seem consistent as the classes are homogeneous and well-delimited, despite the fact that K-means process does not take into account spatial setting.

The classification is missing above areas close to the ground. It is due to the negative log which results from the subtraction of the average deep signal, processed in equation (4). This is happening on areas with shallow depth and extremely low bottom reflectance, such as seagrass [Stumpf et al., 2003]. The signal can therefore be lower than the deep water signal produced by volume scattering.

Table 5 displays the distance between class centroids in the descriptor space. Figures 21 and 22 show the depth repartition of each class, the average and standard deviation of depth and the amount of surface in pixels and in percentage of the total, represented by the class group.

Class 1 seems highly correlated with deep and open-ocean waters. Indeed, the class is mainly set outside of the barrier reef, where bottom surface drops, near the biggest channel through barrier reef (in the study site) named: "Passe De Boulari". Despite the fact that class 1 is certainly more characterized by the optical properties of the water than by the bottom reflectance, due to the depth, this class is well separated from the others in the descriptor space. Its centroid has an average distance of 9.03 from the others. Class 2 is well delimited behind the reef and around islets. With an average distance of 10.49, this is also the most separated class in the descriptor space. It is represented by a restricted range of shallow depth with an average of 7.7 meters. its location, on the back of the reef, seems protected from the daily flow, through the barrier, produced by tides. Class 3 is located on the deep zones of the lagoon. It can be confirmed on Figure 21 which does not shows any shallow depth, smaller than 9-10 meters. It is also visible on the map (Figure 20) as the class is located in front of the channel through the barrier and following deep paleo-valleys. It is specifically visible after the channel around 22.1° South, named: "Passe De Uitoé".

**Figure 21:** Histograms of classes: eight-clusters classification (1)

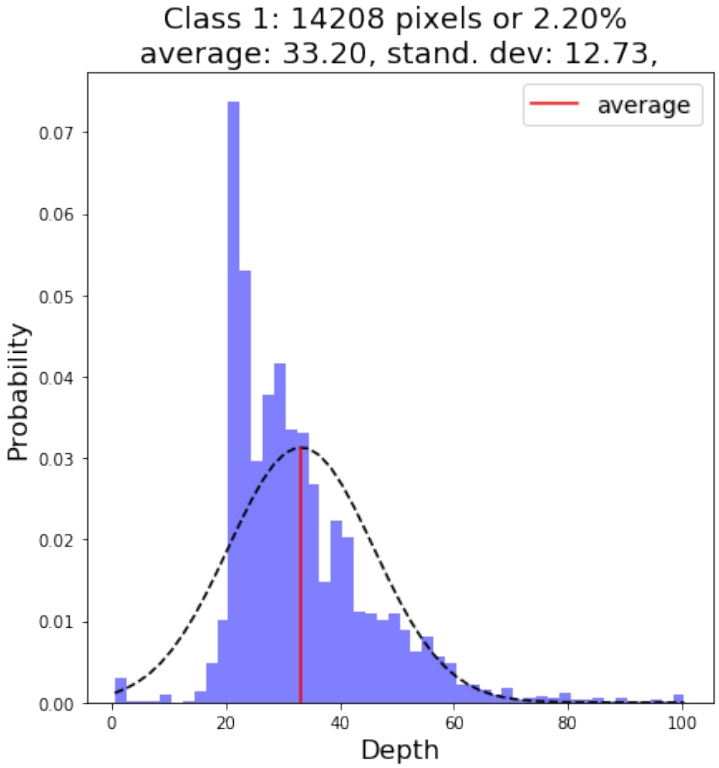


**(a)** Class 1

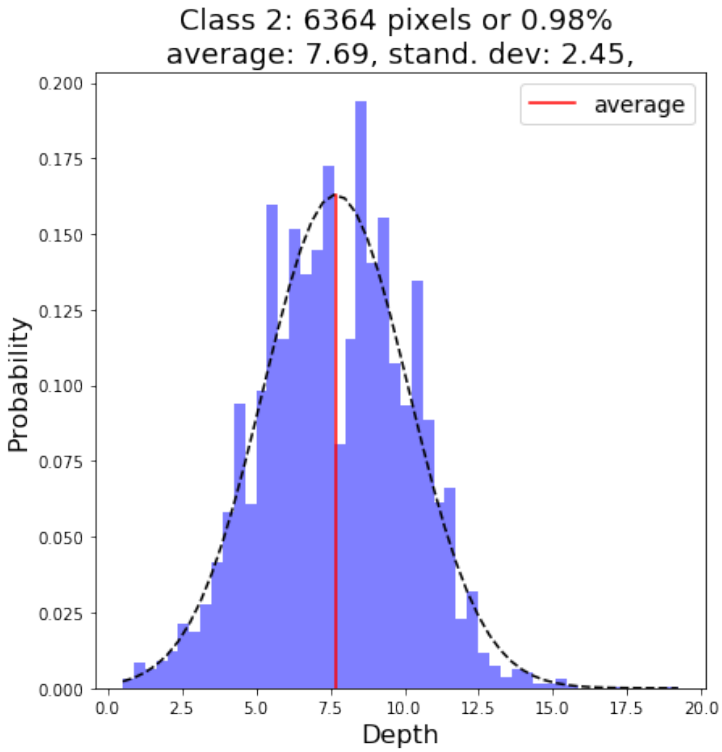


**(b)** Class 2

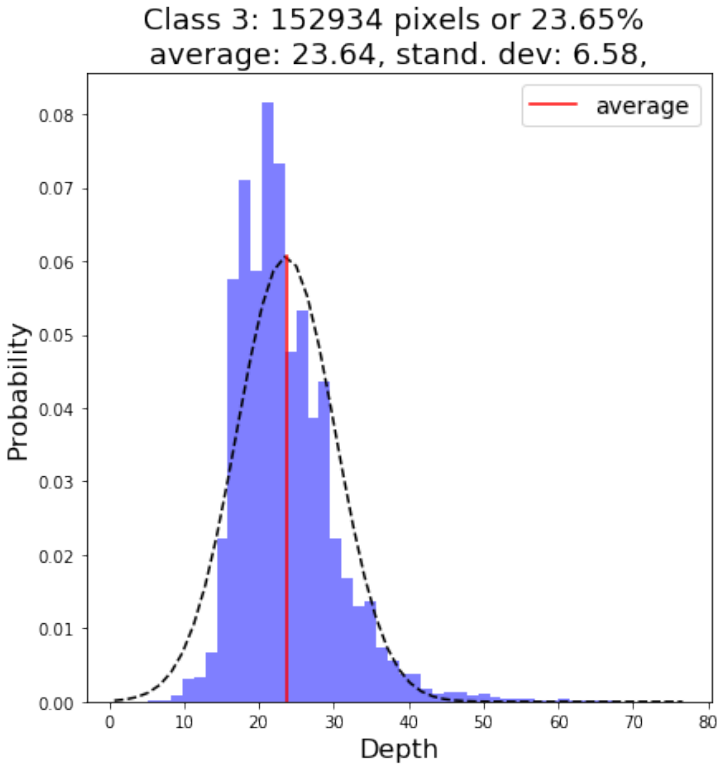


**(c)** Class 3

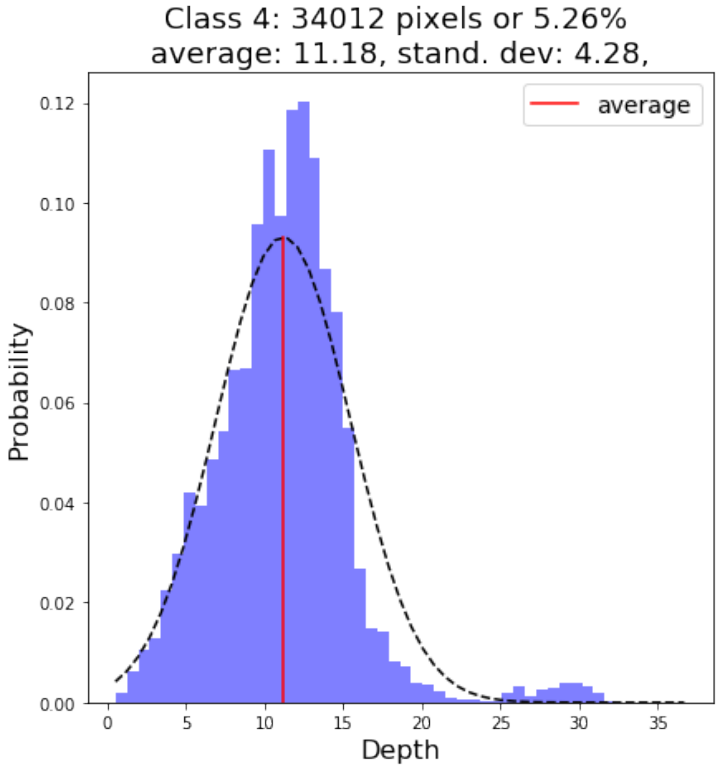


**(d)** Class 4

**Figure 22:** Histograms of classes: eight-clusters classification (2)

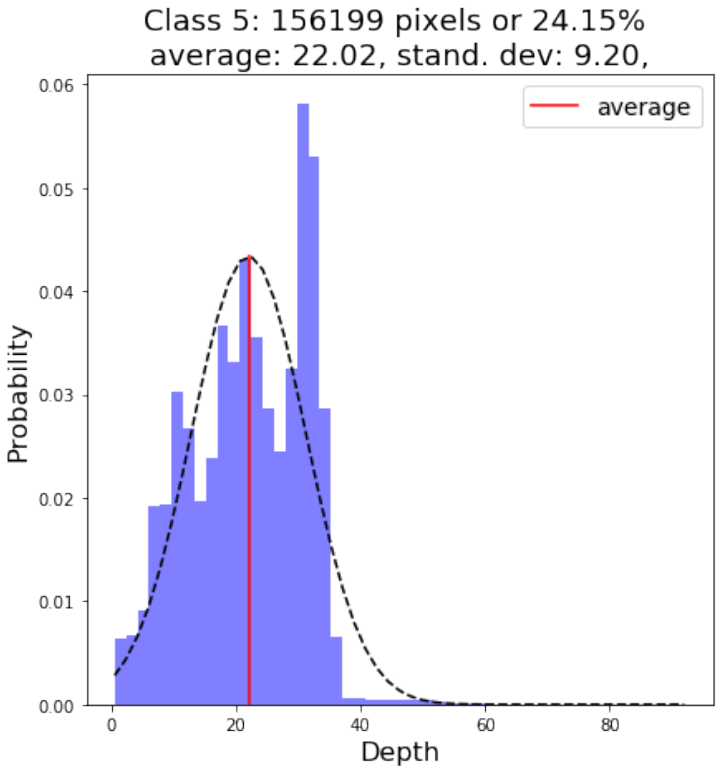


**(a)** Class 5

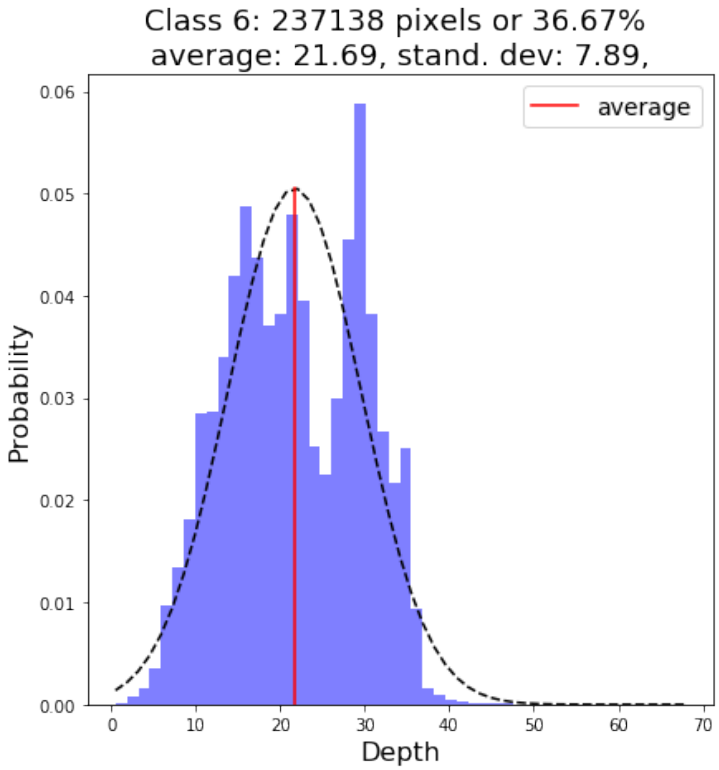


**(b)** Class 6

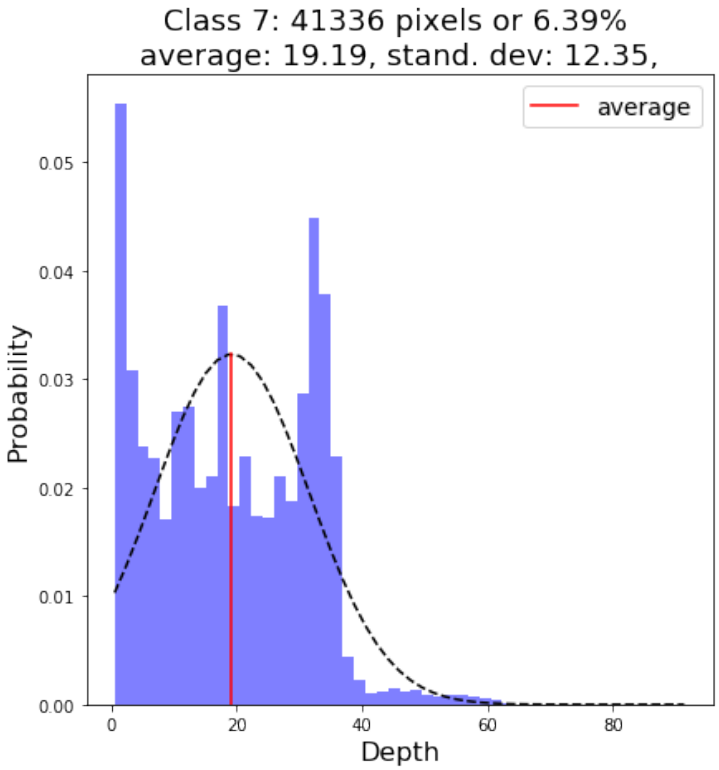


**(c)** Class 7

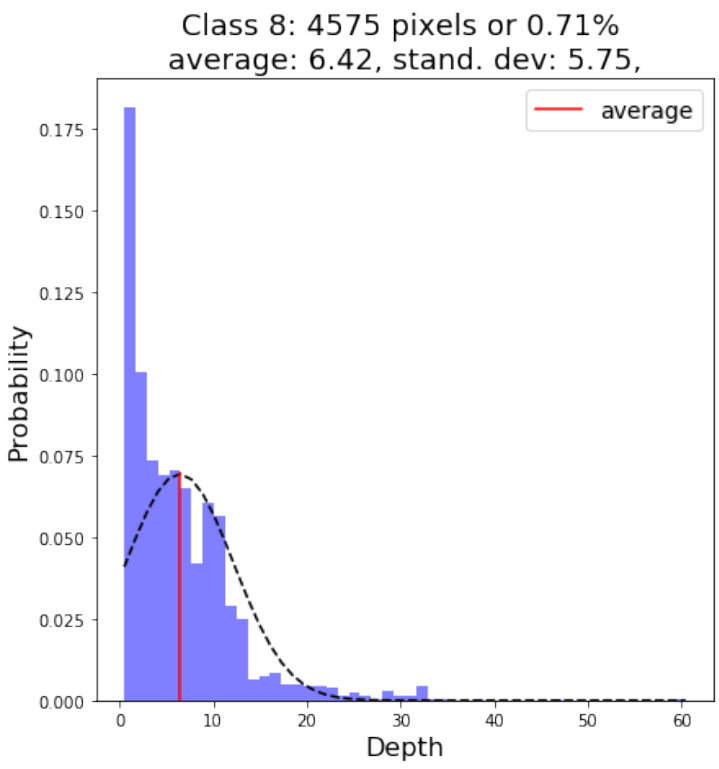


**(d)** Class 8

**Table 5:** Distance matrix from 8 centroids of classification in the descriptors space

| | Class 1 | Class 2 | Class 3 | Class 4 | Class 5 | Class 6 | Class 7 | Class 8 |
|---|---|---|---|---|---|---|---|---|
| Class 1 | 0.0 | 18.84 | 7.74 | 14.49 | 6.22 | 10.43 | 4.40 | 10.08 |
| Class 2 | - | 0.00 | 11.36 | 4.47 | 12.68 | 8.55 | 18.75 | 9.25 |
| Class 3 | - | - | 0.00 | 6.92 | 2.62 | 2.83 | 9.12 | 2.55 |
| Class 4 | - | - | - | 0.00 | 8.42 | 4.12 | 14.80 | 4.83 |
| Class 5 | - | - | - | - | 0.00 | 4.55 | 6.74 | 4.54 |
| Class 6 | - | - | - | - | - | 0.00 | 11.21 | 1.40 |
| Class 7 | - | - | - | - | - | - | 0.00 | 11.20 |
| Class 8 | - | - | - | - | - | - | - | 0.00 |
| Average | 9.027 | 10.49 | 5.39 | 7.26 | 5.72 | 5.38 | 9.53 | 5.48 |

Class 4 is located behind the barrier, around islets and also close to the coast. Classes 5 and 6 are located, on intermediary area, inside the lagoon. Their histograms show great ranges of depth. With class 3 they belong to the less separated classes in the descriptors space with low average distance. These 3 classes are indeed close from each other in descriptors space. Class 7, is the closest from the areas with negative log signal. It shows a big range of depth but also a large area of shallow bottom. Finally, class 8 is clearly located on barrier reefs and wave-cut platforms. These areas are typically shallow, which is confirmed by its histogram on Figure 21. As shown by the figure, these areas, represent an extremely small part of the pixels containing measurements. With a total of 4575 measured pixels, these areas with extremely irregular and shallow bottom are indeed hard to measure by boat as it is difficult to sail in.

**Table 6:** Distance matrix from 3 centroids of classification

| | Class 1 | Class 2 | Class 3 |
|---|---|---|---|
| Class 1 | 0.0 | 13.26 | 6.57 |
| Class 2 | - | 0.00 | 7.09 |
| Class 3 | - | - | 0.00 |
| Average | 6.61 | 6.78 | 4.55 |

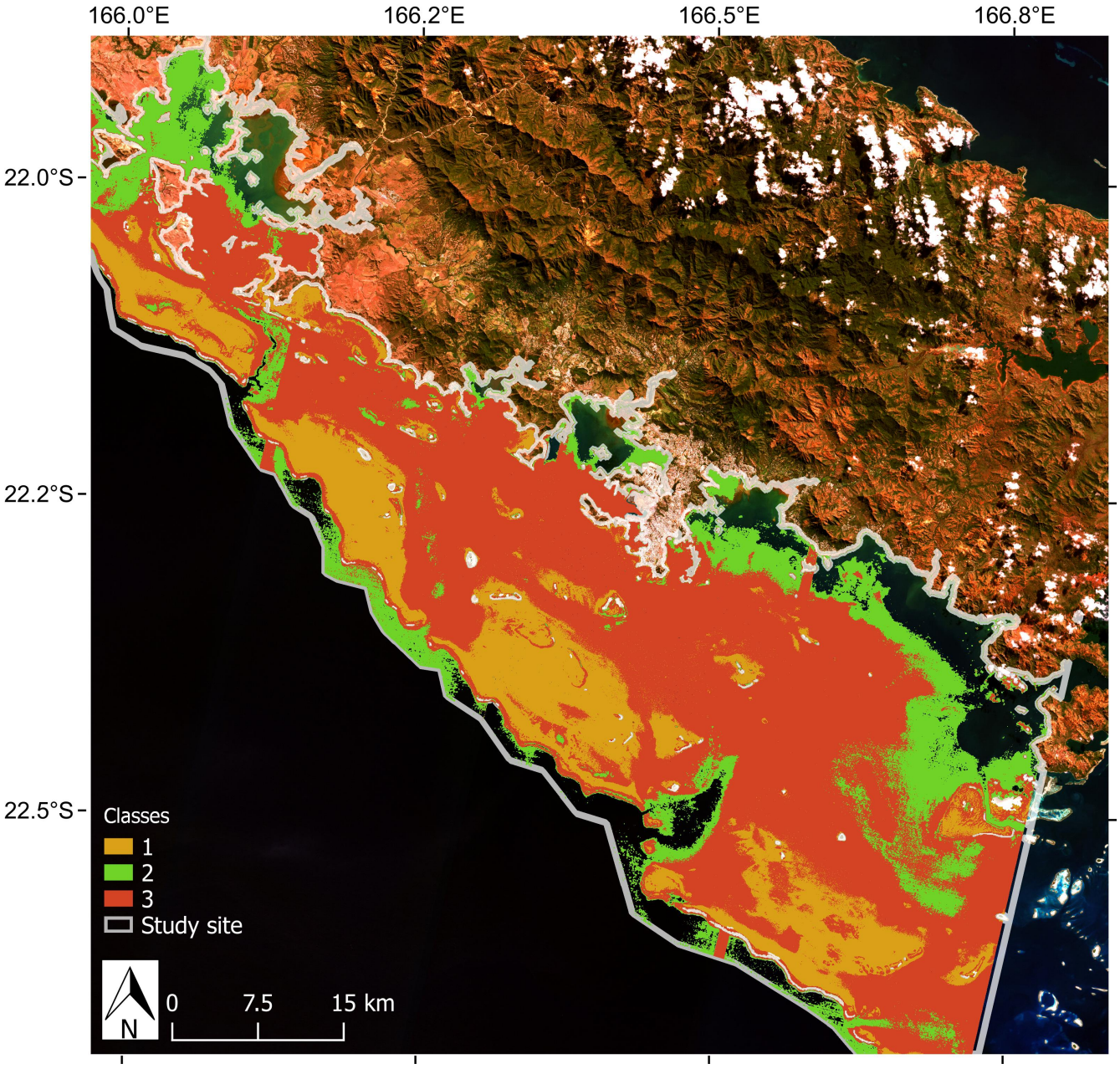


**Figure 23:** Classification in 3 clusters following bottom reflectances and water properties

The three clusters classification map, visible on Figure 23 and distance matrix visible in Table 6, in the annex, are harder to comment. Class 1 represents mainly areas which are on the back of the barrier, maybe less exposed to the daily tidal flow. Class 2 relates to areas that are close to the coast and to outside barrier areas simultaneously. It results in a great range of depth in the class. Class 3 is located on an intermediary area and on the reef itself. Class 3 is the most represented, with 483'265 pixels, containing in-situ measurements, as observations, it represents 74.72% of the dataset.

## 3.6 Depth models

**Table 7:** Validation: Performances of the best models

| Model | | | Lyzenga | | | | Stumpf | | | |
|---|---|---|---|---|---|---|---|---|---|---|
| Score | | | $R^2$ | Error[m] | Max. D. | Max. V. | $R^2$ | Error[m] | Max. D. | Max. V. |
| Large site | 8 c. | 1 | 0.77 | 2.4 | 20 | 54 | 0.84 | 2 | 20 | 54 |
| | | 2 | 0.80 | 0.6 | 10 | 94 | 0.78 | 0.6 | 10 | 98 |
| | | 3 | 0.37 | 1.1 | 20 | 73 | 0.27 | 1.2 | 20 | 50 |
| | | 4 | 0.85 | 0.9 | 20 | 99 | 0.82 | 1 | 20 | 99 |
| | | 5 | 0.57 | 2.5 | 20 | 10 | 0.59 | 2.4 | 20 | 62 |
| | | 6 | 0.59 | 1.9 | 20 | 10 | 0.55 | 1.9 | 20 | 99 |
| | | 7 | 0.75 | 3.5 | 30 | 55 | 0.75 | 3.5 | 30 | 55 |
| | | 8 | 0.71 | 2 | 30 | 80 | 0.66 | 2.2 | 30 | 84 |
| | 3 c. | 1 | 0.85 | 0.9 | 20 | 71 | 0.81 | 1.1 | 20 | 71 |
| | | 2 | 0.73 | 1.6 | 15 | 10 | 0.79 | 2.6 | 25 | 100 |
| | | 3 | 0.61 | 1.9 | 20 | 50 | 0.60 | 2 | 20 | 50 |
| | 1 c. | - | 0.62 | 2.8 | 25 | 96 | 0.65 | 1.6 | 15 | 83 |
| Small site | 3 c. | 1 | 0.83 | 0.9 | 15 | 99 | 0.80 | 0.9 | 15 | 99 |
| | | 2 | 0.80 | 3 | 30 | 100 | 0.82 | 3 | 30 | 88 |
| | | 3 | 0.63 | 2.1 | 20 | 10 | 0.59 | 2.6 | 25 | 10 |

After the fitting and the research of the maximum optimal depth and optimal variance as parameters for filtering the training dataset, the best models are selected on the basis of the performances, resulting from a kfold cross-validation. As explained in the section 2.8.2, this selection process is performed with 4 folds. Once the selection process is achieved, the best models are trained one last time with 20 folds, in order to produce validation results. These results aims at estimating as closely as possible the range of error which would occur on new unknown data, in other word on pixels without in-situ measurements. To this end, the validation process named "leave one out", consisting in predicting every observation of the dataset with a model trained on all others observations, would be the most effective one. However, with such a number of measured pixels as

observations, it would require a considerable time of computation. For these reasons, validation results are produced with twenty models predicting each one twentieth of the dataset. Table 7 summarizes the validation performances.

Results displayed on Table 7 with Stumpf's model are performed with the usual combination of the green and blue band as unique descriptors. However, as the correlation with depth are higher with the combination of the green and additional shorter blue band, this second option has also been tested. Table 8, in the annex shows a comparison between validation performances produced with the usual Green/Blue combination and the Green/Short blue combination. To sum up, despite a lower correlation with depth, the usual combination stays slightly better. It is important to keep in mind that the Shorter blue band used here, results from a down scaling with an original resolution of 60 meters. Despite the weakness of Stumpf's method with low ground resolution (see section 2.7.2), results remain fully comparable. The combination of a green band with a 10 meters ground resolution with a shorter blue band with a 60 meters resolution but higher penetration ability in water seems to overcome this weakness.

The eight-clusters classification produce the highest results with Stumpf with a score of 0.84 on class 1 and 0.82 on class 4. With Lyzenga's model, the best results are similar between the eight-clusters classification and the three-clusters classification with two equal score of 0.85 for class 4 and class 1. On the opposite, eight-clusters classifications also give the worst scores, on class 3. Models without any classification result in middling scores of 0.62 and 0.65. No really improvement of the predictions happen as the models are restricted to the small site, which is the detector's footprint containing the selected sample used for the computation of DII.

The ranges of error seems highly correlated with the optimal predictable depth. Regarding the models having the same optimal predictable depth, lyzenga's model give slightly smaller errors but both models' error are really close.

With a high number of clusters, both models are optimally predicting up to the same maximum depth. With a smaller number of clusters or without any classification, Lyzenga's model seems more sensitive and shows shallower optimal maximum depths. The overall results also tend to show a stricter depth variance filtering with this model.

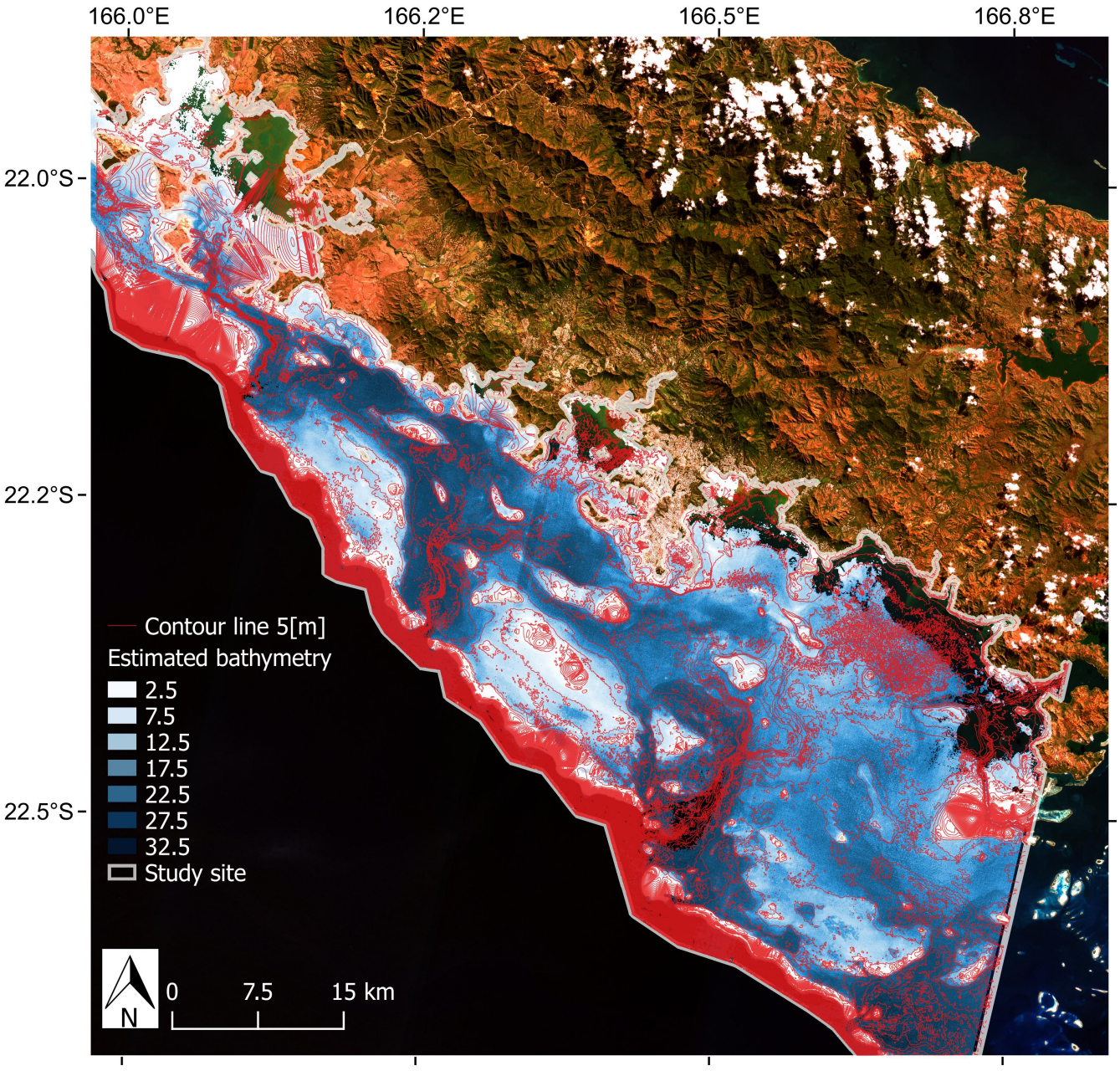


**Figure 24:** Bathymetry predicted by a three clusters-classification Lyzenga's model with 5 meters contour line produced after interpolation of all in-situ measurements. The color range allows a direct comparison with the contour lines

Figure 24, shows the final bathymetry map predicted by a Lyzenga's model and calibrated on the overall dataset, filtered with the optimal parameters (displayed in Table 7) after a three-clusters classification. Contour lines are computed on the basis on the interpolation of all in-situ measurements without any filtering. This interpolation is visible in the annex in Figure 4. By comparison with the contour lines, the predicted bathymetry generally seems coherent up to approximatively 22 meters. Predictions on deeper bottom seem more noisy. For instance, paleo-valleys, are hard to observe on the predictions map. The Southern part of the study site, which is

a more open area, seems to display especially random predictions.

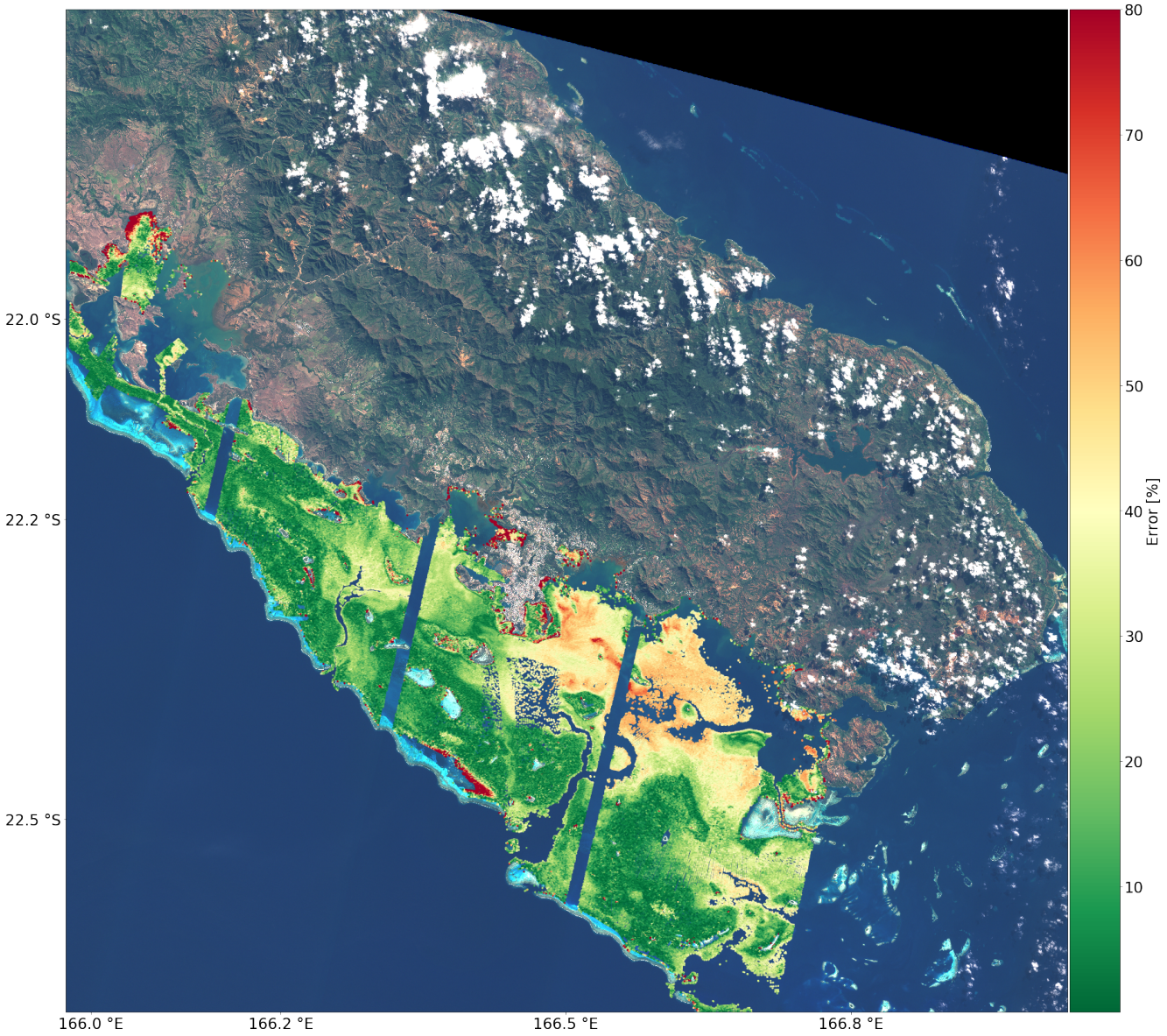


**Figure 25:** Scatter of validation error in percent, produced with 20 folds on a Lyzenga's model with 3 classes

Figure 25, shows a scatter map of the validations error of a Lyzenga's model after a three-clusters classification. The resulting error, generally remains under 40 %. Nevertheless, the error above shallow depth can increase brutally. High error occurs nears the unclassified zones, which correspond to negative logarithm of the recorded signal. High error, also occurs close to the coasts, especially in the Northern bay, called "bay of Saint- Vincent". Results are also decreasing in the Southern part of the study site. This part corresponds to a more open areas with potential different dynamic of flows.

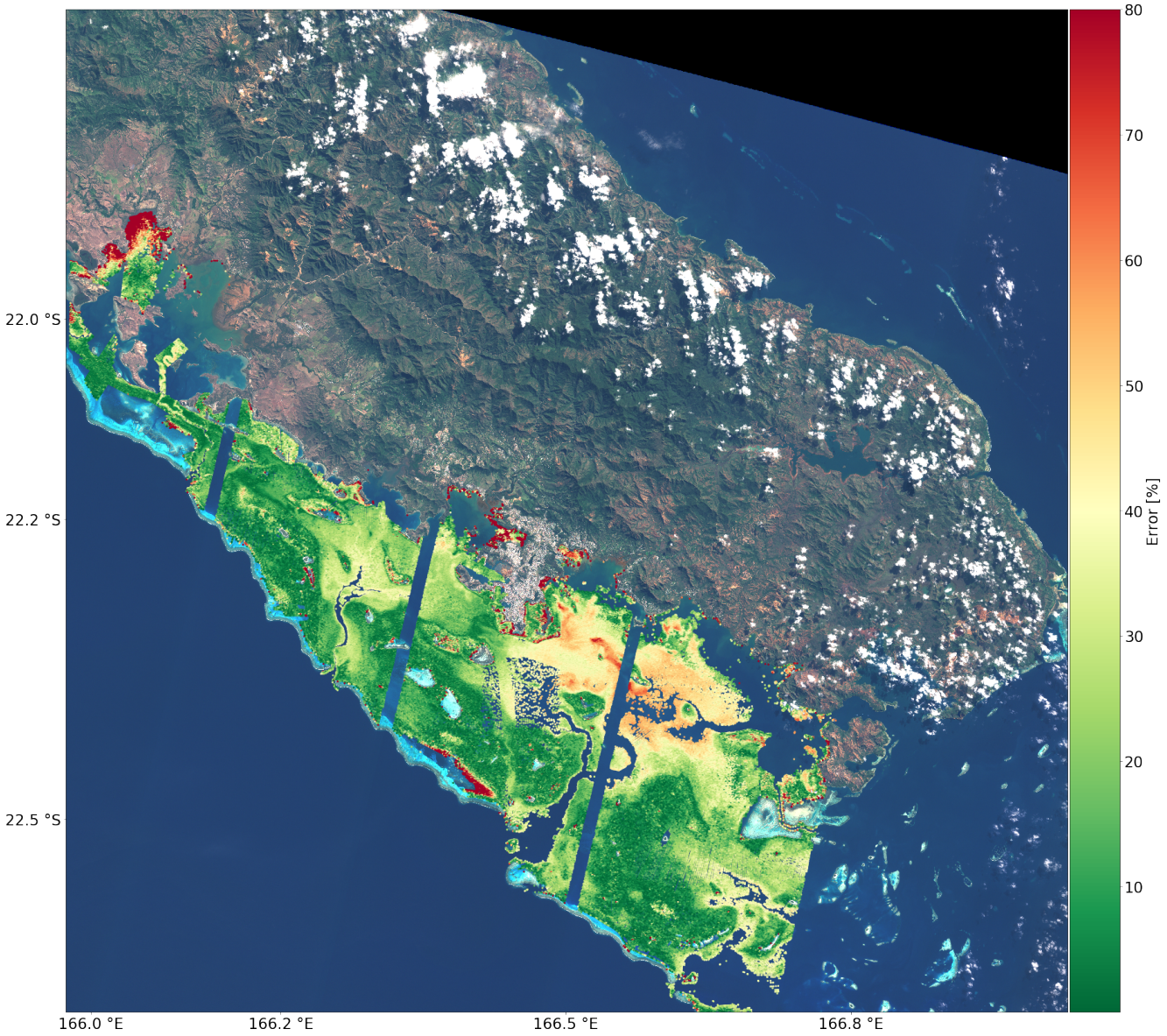


**Figure 26:** Scatter of validation error in percent, produced with 20 folds on a Lyzenga's model with 8 classes

Figures 26 and 27 show the same validation map achieved respectively with Lyzenga's and Stumpf's model after an eight-clusters classification. These two additional maps allow to confirm the systematic errors occurring as the localization get closer to the coasts or to the Southern part. The errors occurring in the Northern bay are increasing with the eight-clusters classification compared to the three-clusters classification. Stumpf's model after an eight-clusters classification, shows larger amount of surfaces having 40 % or more of error.

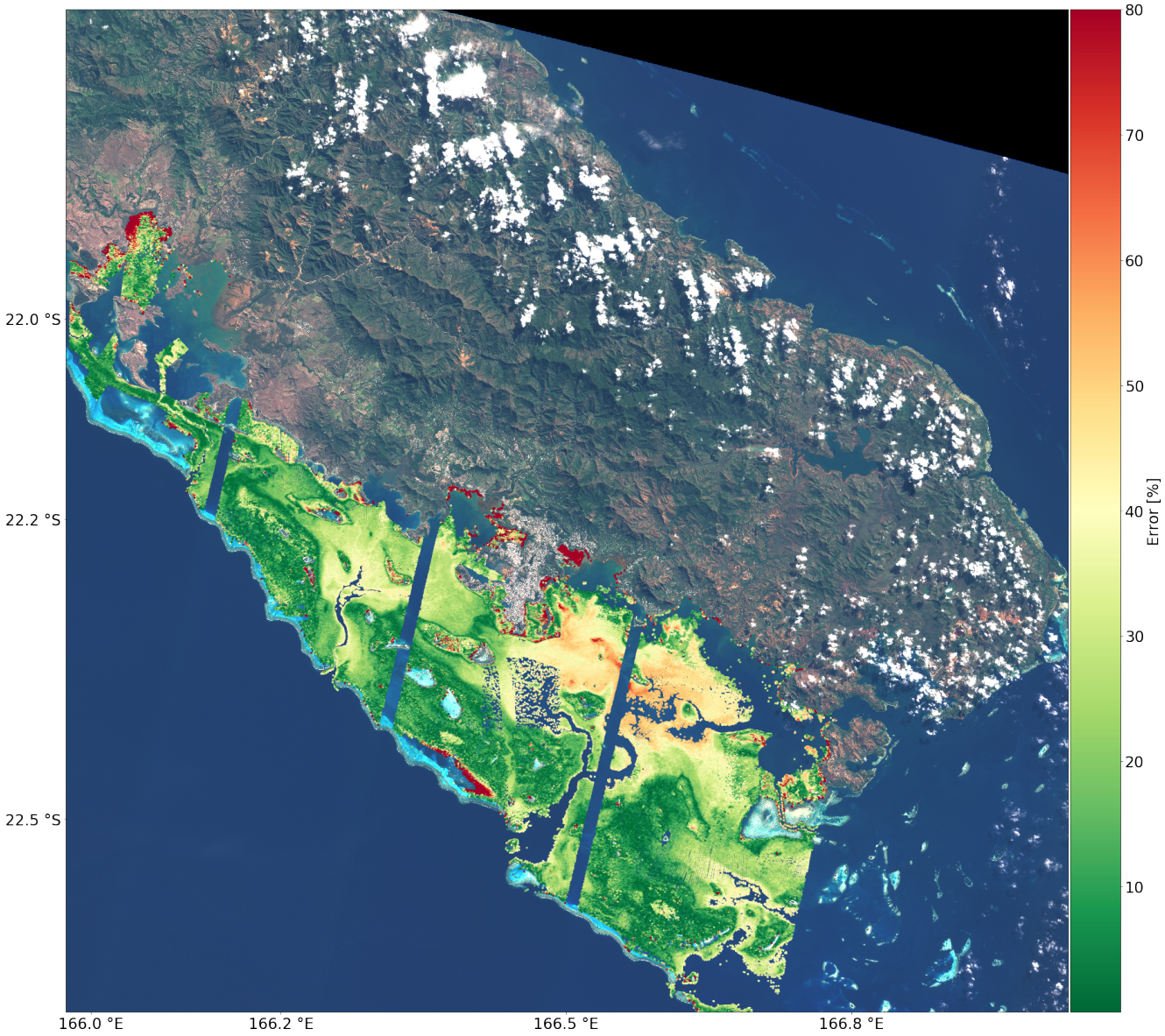


**Figure 27:** Scatter of validation error in percent, produced with 20 folds on a Stumpf's model with 8 classes

# 4 Discussion

Regarding Table 1, variable results are expected after the application of empirical modeling for satellite derived bathymetry. The prediction depth observed in literature goes from 10 meters in unfavorable case, to 25 meters in favorable case. Mean absolute error is about 1.65 meter to 3 meters. In our results, the maximum prediction depth is at least of 10 meters and can rise up to 30 meters in favorable case with classification. The best mean absolute error observed is less than 1 meter. Indeed, class 2 of the eight-clusters classification has a mean error of 60 centimeters. However, its maximum prediction depth, up to 10 meters, is really low. On the opposite, the worst mean error is observed on classes having maximum prediction depth of 30 meters, which is superior to the study case observed in literature. To sum up, the results of this study are in the range of the expectations.

## 4.1 The distance from coasts as a suitable condition ?

Regarding the validation map, visible in Figure 25, it appears that areas lying close to the coasts have systematically higher errors. Indeed, depths are shallower, which make the errors increase if it is measured as percent. However, areas close to islets and reef, which has also shallower depths, does not show such a systematic error. With this in mind, the water clarity, far from the coasts, can be supposed higher. Water run-off from coasts to ocean can be responsible for an increase in turbidity which make the prediction of depth harder.

## 4.2 The Choice of the model

Figure 28 shows a comparison between the two models. Lyzenga's performances, most of the times, appears to slightly improve predictions. Class 1 from eight-clusters classification, located in deep and open-ocean water, has better results with Stumpf. Similarly, class 2 from three-clusters classification, which is also located on area close to negative log signal zone, shows a better performance with Stumpf's model. Regarding the optimal depth, performances are globally the same for the two models except in three situations. Class 2 on three-clusters classification, on the large site, is optimally predicted up to 25 meters by Stumpf and only up to 15 meters by Lyzenga. Class 3 on three-clusters classification on the small site, is optimally predicted up to 25 meters by Stumpf and only up to 20 meters by Lyzenga. Nevertheless, the models without classes give an advantage to Lyzenga which can optimally perform on 10 meters more. Finally, Lyzenga's models seem a bit more sensitive to the variation of depth in a training pixel or a pixel representing slope. Their maximum variances are indeed often lower than those of Stumpf's model. The Parameter of variance filtering can be strict.

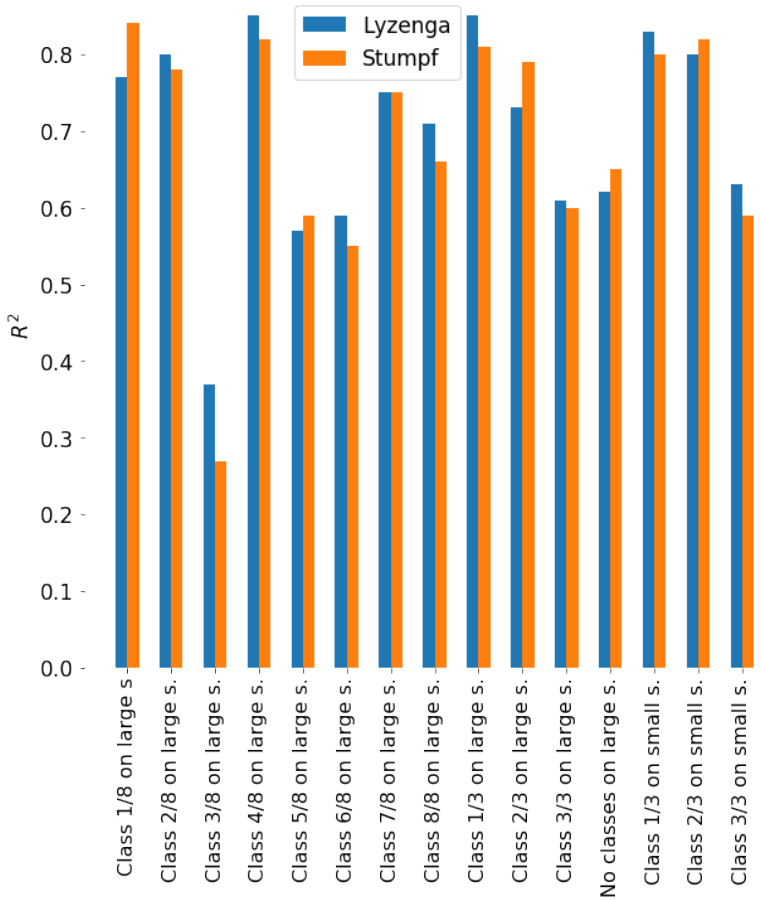


**Figure 28:** Comparison of performance between model types

Comparisons between Lyzenga's and Stumpf's model show some close results. To sum up the overall performances, Lyzenga's model can be evaluated as slightly better, despite some exceptions. As an example, without any classification, Stumpf's model gives better results. Maximum depth of prediction is approximately the same. Despite the weakness of noise sensitiveness of Stumpf's model, described in literature (see section 2.5.1), the model is less demanding regarding variance filtering of the training dataset. Furthermore, with its two-bands combination as unique descriptor, it has to be noticed that Stumpf's model is much simpler. Consequently, it is likely less over-fitted. It may lead the errors computed among the 20 folds of validation to be more stable, which could explained the higher tolerance of Stumpf's model regarding variance filtering of the training dataset.

## 4.3 The classification as initial step

Figure 29 shows a comparison between classification approaches. For each classification, an average $R^2$ ,weighted by the area of each cluster, is computed. Resulting average scores are visible as barplot. Regarding the figure, a classification approach, based on a small number of major classes, seems to improve the global results. Nevertheless, a high number of divisions of the dataset de-

creases the performances. Indeed, Lyzenga's model reaches an average of 0.68 with a three-clusters classification, whereas it performs only a score of 0.62 without classification. Eight-classes classification is limited to 0.61 with Lyzenga's model. Three-clusters classification with Stumpf's model gives a maximum score of 0.67 whereas its score is of 0.65 without any classification and of 0.58 with a eight-classes classification. Regarding classifications maps on Figures 20 and 23, class 4, from the eight-clusters classification, and class 1, from the three-clusters classification, can be compared as they are located in the same areas and represent comparable faction of the dataset. Using Lyzenga's model, the results are similar. Using Stumpf's model, the eight-clusters classification give a tiny improvement of the $R^2$ score and an average error is lowered from 0.1 meter.

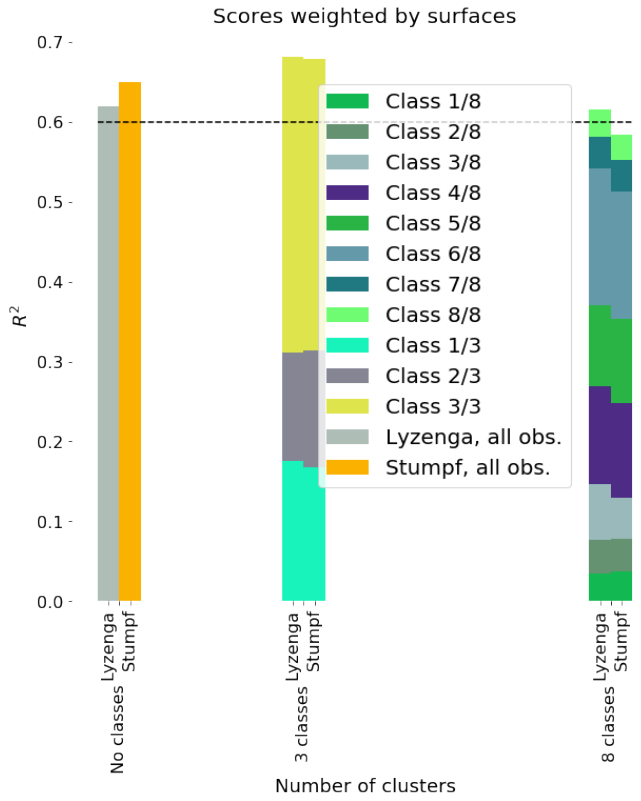


**Figure 29:** Comparison of performances between classifications approaches

The classification approach aims at creating sub-datasets whose remaining variance are due to depth variation. As explained in section 2.6, the choice of the number of clusters is a delicate task. Results show that it is also a crucial one. Indeed, a too high number of divisions of the dataset does not allow to improve the result. On the contrary, it produces poorer results. However, a small number of divisions, allows an improvement of the performance. The clustering of the dataset until the acquisition of interpretable classes is disadvantageous for the predictions' accuracy. The observations have to be clustered only by their primary dissimilarities regarding their optical properties translated by the descriptors. Nevertheless, the classification of the dataset allows to isolate classes having better conditions for satellite derived bathymetry which can reach larger maximum depth.

## 4.4 The application scale

Finally, Figure 30 allows a comparison of the performances following the scale of application of the model.The small site designates models which are fitted on the basis of observation, selected only on the detector's footprint containing the sample which has served to generate DII (Section 2.5.1). The large site refers to the global study site. Regarding the figure, it is not possible to highlight significant differences between these two scales.

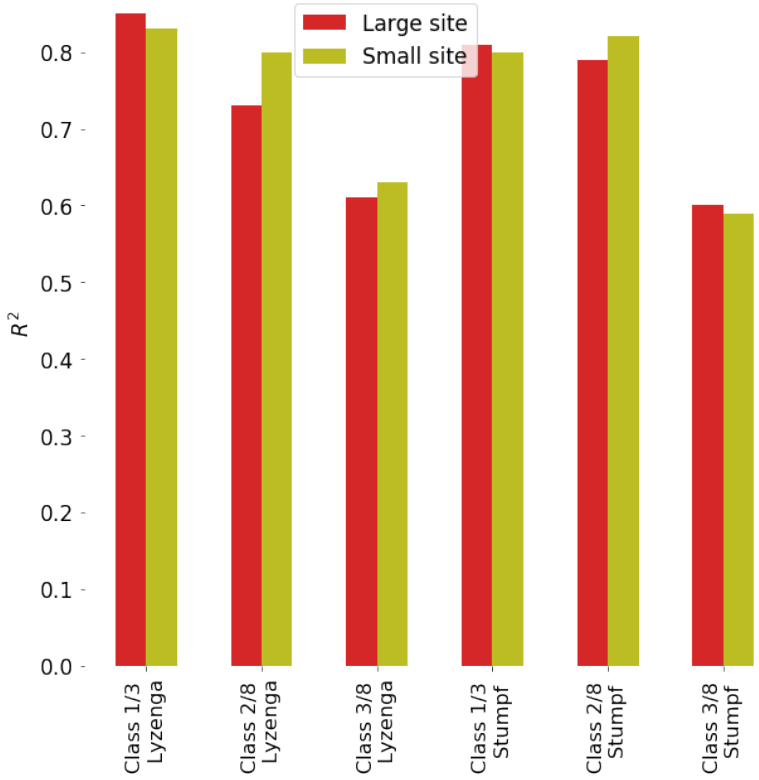


**Figure 30:** Comparison of performances between scale of application

As explained in section 1.2, the method's application scale is an important question as it is one of the main advantage of satellite derived bathymetry. Regarding Figure 30, there is no systematic difference between the performances of models trained and tested on the unique footprint containing the sample used for the creation of the DII and the performances of models trained and tested on the overall study site. Consequently, nothing seems to prevent the application of the empirical methods on a extended area. A preprocessing, such as glint removal, applied individually on each detectors footprint allows to extend the depth model calibration to every detectors. In addition, the scatter of validation error, visible in Figure 25 does not show any relations between errors and distances from the sample, used for the computation of DII. The classification seems, therefore, consistent on the large extent of the study site. However, the scatter of errors, seems more related to the distance from the coasts. In addition, let us notice that the study site of this work is continuous. It can not be certain that performance would be the same in case the North East coast of New Caledonia were to be inserted in the study site.

# 5 Conclusion

This thesis investigated the potential of empirical modelings, applied to images provided by the Sentinel-2 sensor, in order to make large scale predictions of the bathymetric landscape. Despite the use of several detectors in order to produce an images, this sensor, with an appropriate methodology, can provide a suitable tool for the estimation of gaps in bathymetric charts. It allows to produce bathymetric map, sampled on a regular grid, including shallow coral areas, which are difficult to measure by boat. For this reason, satellite derived bathymetry can provide a valuable alternative for researchers needing to study coral ecosystems.

## 5.1 Achieved results

In this work, several results were achieved :

- The ability of Sentinel-2, still rarely used in oceanic remote sensing, for mapping the bathymetric landscapes has been demonstrated. The overall performances of empirical methods lies within the ranges observed in literature.
- An approach based on classification as an initial step, aims at isolating variance driven by depth, was assessed. Results shows an improvement of models calibrated on large primary classes of the dataset.
- The possibility to calibrate models at the scale of an image and produce depth predictions over a large extent has been demonstrated and validated.
- The errors estimates produced by empirical modeling were found to be strongly spatially correlated and influenced by their situations with respect to the coasts, which lead to variations of the waters' optical properties.

## 5.2 Future work

Several ways of development remain to be tested in order to improve the accuracy of this methodology:

- The insertion of areas having a negative logarithm signal in the classification followed by a depth prediction relying on Stumpf's descriptor, to extend the estimated map.
- The realization of in-situ measurements of bottom type in order to safely select homogeneous sample for the DII computation .
- The fusion of the Lyzenga's and Stumpf's model descriptors with the insertion of a parameter of penalization of complex model, in regressions such as Ridge or Lasso regression.
- The insertion of a step, aims at removing outliers from the dataset. An additional, initial, classification process such as, density-based spatial clustering of applications with noise could be achieved to highlight outliers.

# 6 ANNEXE

**Figure 31:** Histograms of classes: three-clusters classification

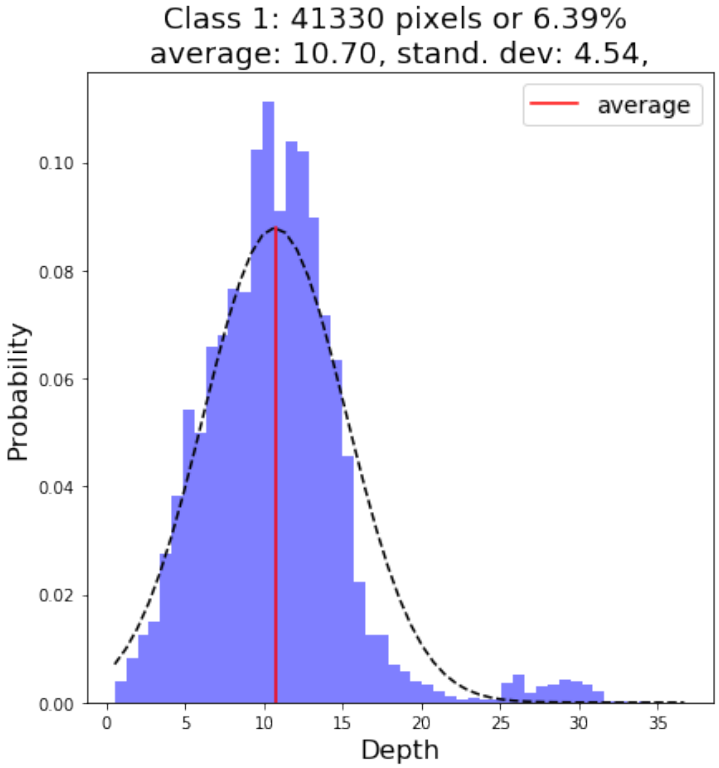


**(a)** Class 1

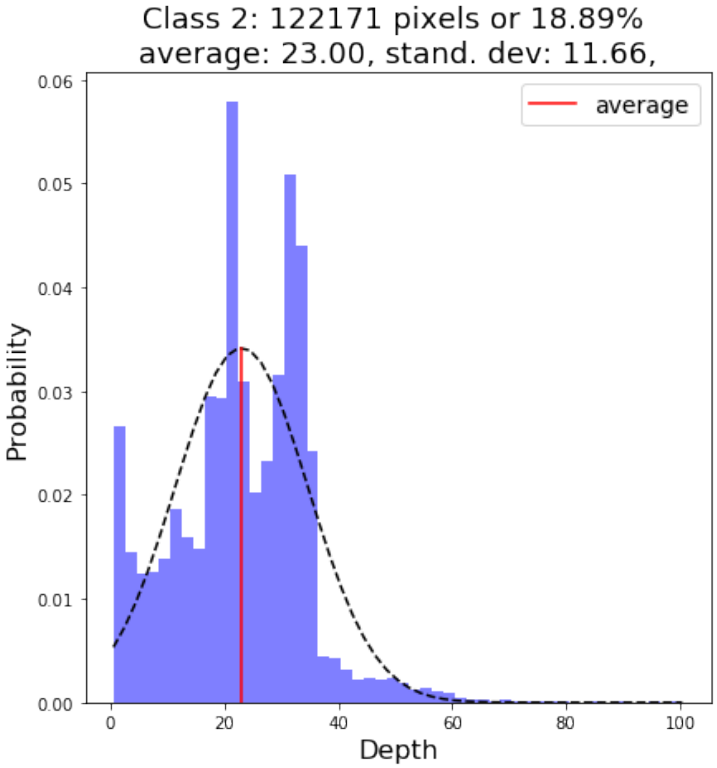


**(b)** Class 2

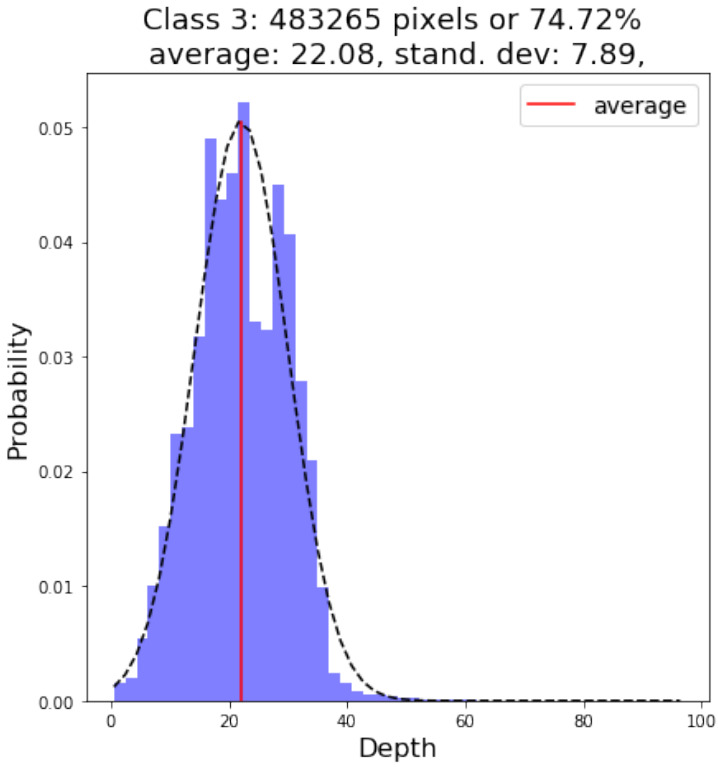


**(c)** Class 3

**Table 8:** Validation: Comparison with the use of shorter blue band in Stumpf's model

| Model | | Stumpf (Green/Blue) | | | | Stumpf (Green/ShortBlue) | | | |
|---|---|---|---|---|---|---|---|---|---|
| Score | | $R^2$ | Error[m] | Max. D. | Max. V. | $R^2$ | Error[m] | Max. D. | Max. V. |
| Large site | 8 c. | | | | | | | | |
| | 1 | 0.84 | 2 | 20 | 54 | 0.81 | 2.21 | 20 | 54 |
| | 2 | 0.78 | 0.6 | 10 | 98 | 0.73 | 0.7 | 10 | 99 |
| | 3 | 0.27 | 1.2 | 20 | 50 | 0.30 | 1.16 | 20 | 59 |
| | 4 | 0.82 | 1 | 20 | 99 | 0.77 | 1.2 | 20 | 100 |
| | 5 | 0.59 | 2.4 | 20 | 62 | 0.55 | 2.5 | 20 | 63 |
| | 6 | 0.55 | 1.9 | 20 | 99 | 0.50 | 2 | 20 | 10 |
| | 7 | 0.75 | 3.5 | 30 | 55 | 0.74 | 3.5 | 30 | 55 |
| | 8 | 0.66 | 2.2 | 30 | 84 | 0.54 | 2.68 | 30 | 85 |

**Figure 32:** Silhouette plots achieved with sci-kit learn Package [Buitinck et al., 2013] on two randomly selected dataset of 3000 pixels (1)

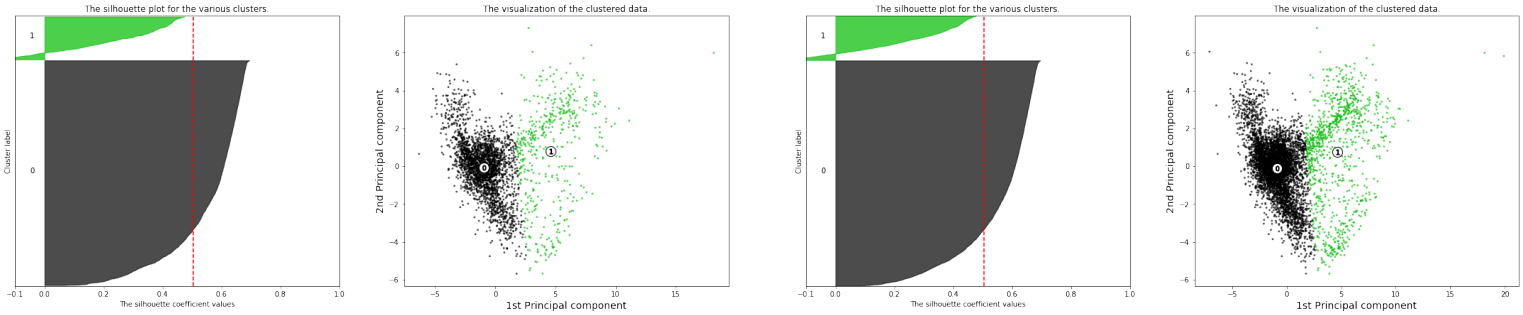


**(a)** Dataset 1: 2 clusters




**(b)** Dataset 2: 2 clusters

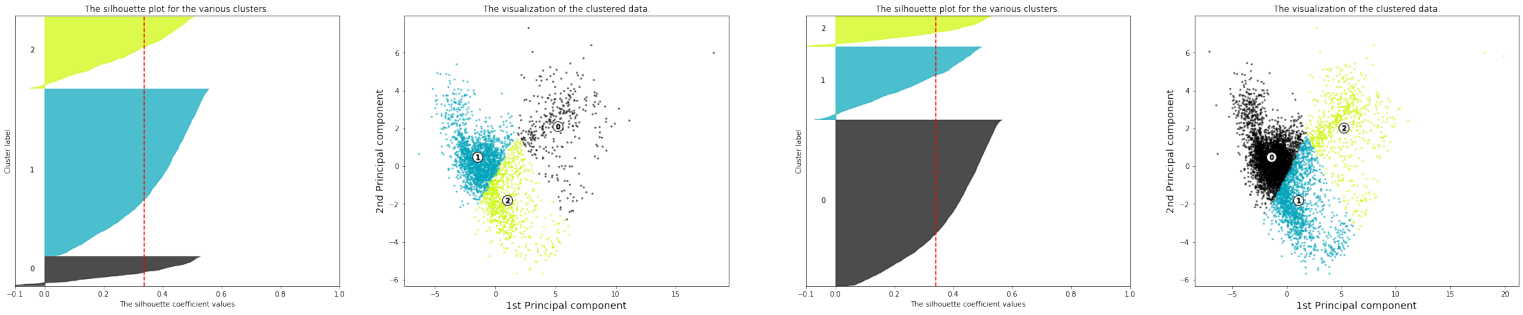


**(c)** Dataset 1: 3 clusters




**(d)** Dataset 2: 3 clusters

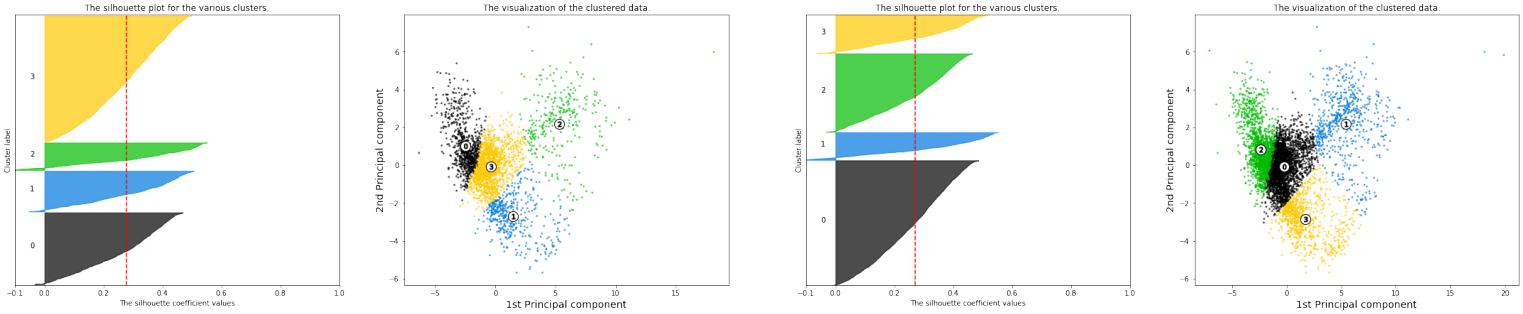


**(e)** Dataset 1: 4 clusters




**(f)** Dataset 2: 4 clusters

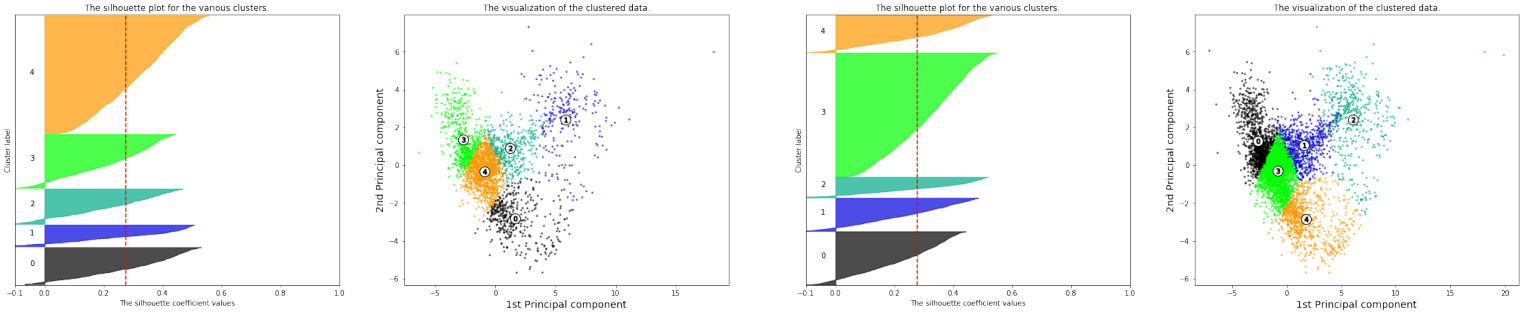


**(g)** Dataset 1: 5 clusters




**(h)** Dataset 2: 5 clusters

**Figure 33:** Silhouette plots achieved on two randomly selected dataset of 3000 pixels (2)

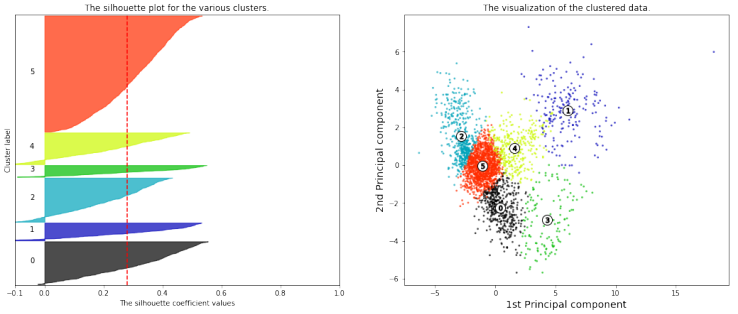


**(a)** Dataset 1: 6 clusters

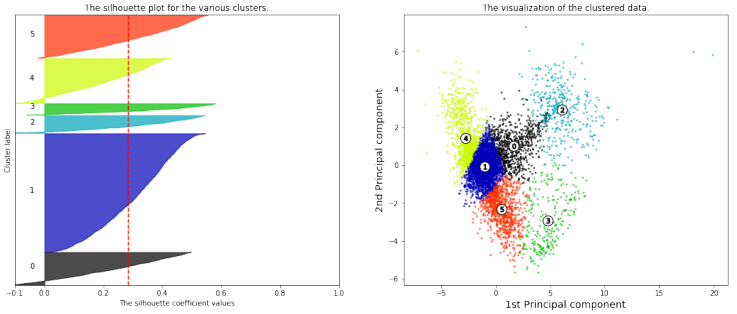


**(b)** Dataset 2: 6 clusters

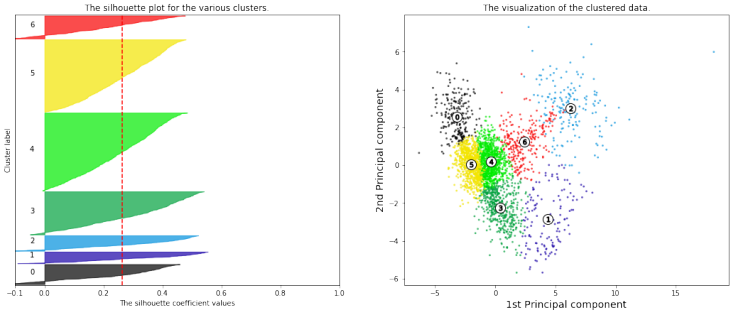


**(c)** Dataset 1: 7 clusters

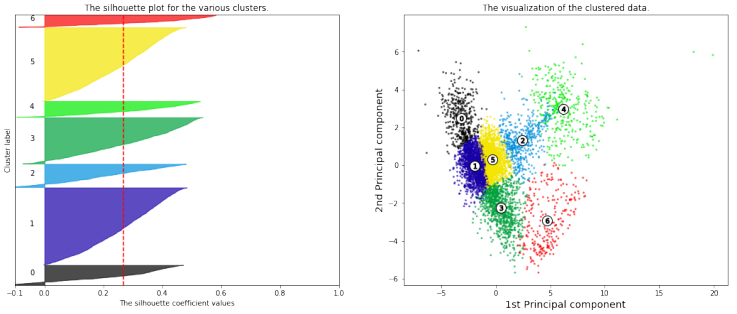


**(d)** Dataset 2: 7 clusters

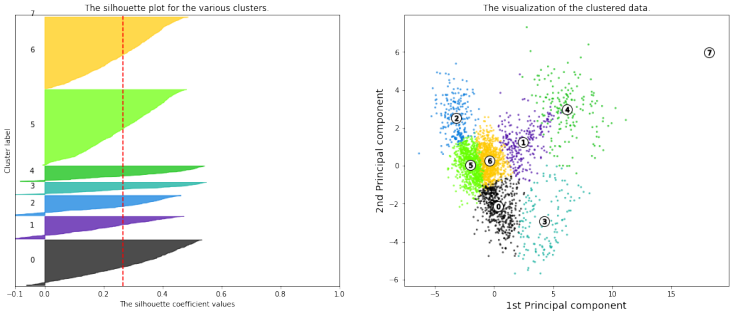


**(e)** Dataset 1: 8 clusters

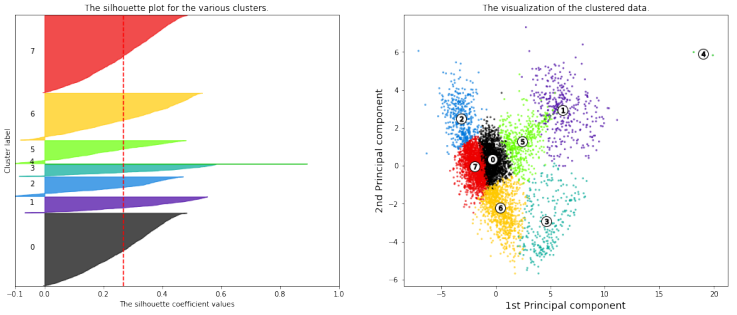


**(f)** Dataset 2: 8 clusters

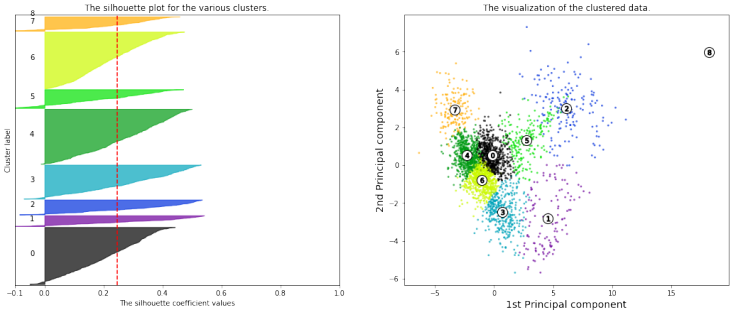


**(g)** Dataset 1: 9 clusters

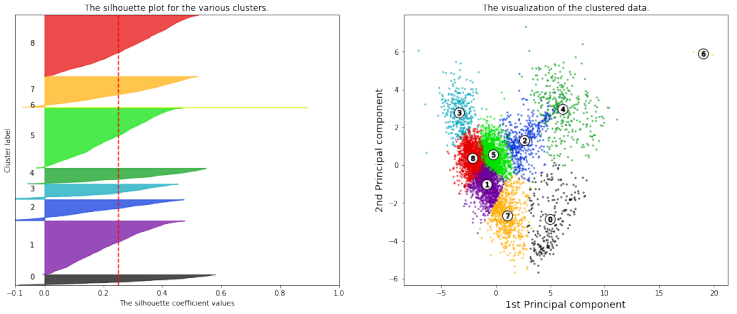


**(h)** Dataset 2: 9 clusters

**Figure 34:** Silhouette plots achieved on two randomly selected dataset of 3000 pixels (3)

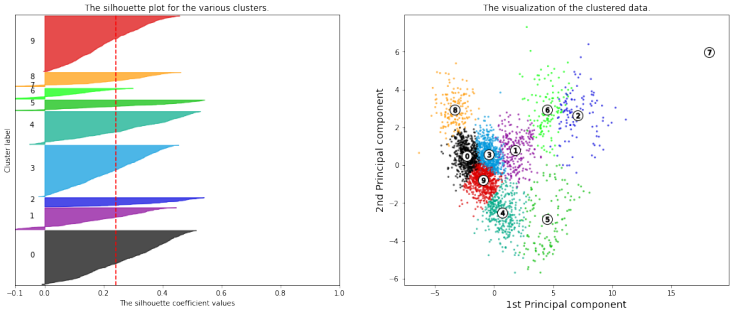


**(a)** Dataset 1: 10 clusters

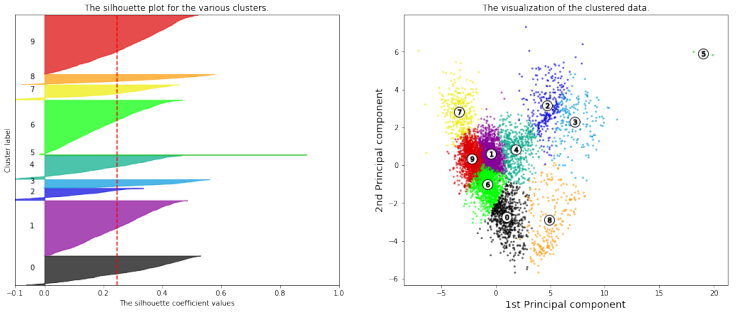


**(b)** Dataset 2: 10 clusters

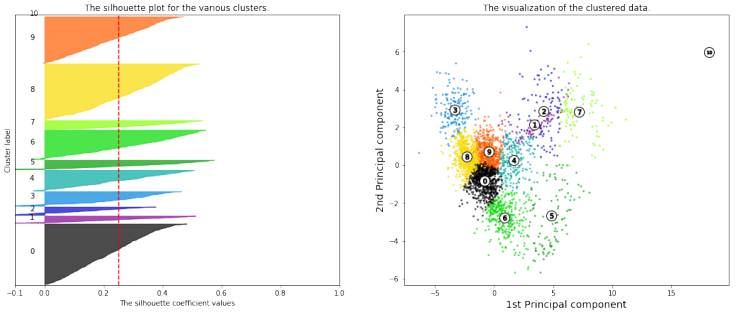


**(c)** Dataset 1: 11 clusters

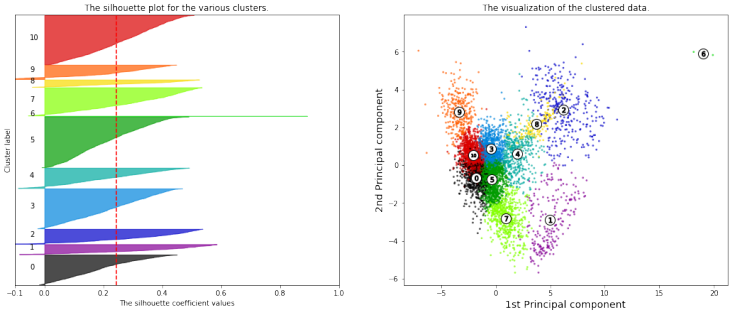


**(d)** Dataset 2: 11 clusters

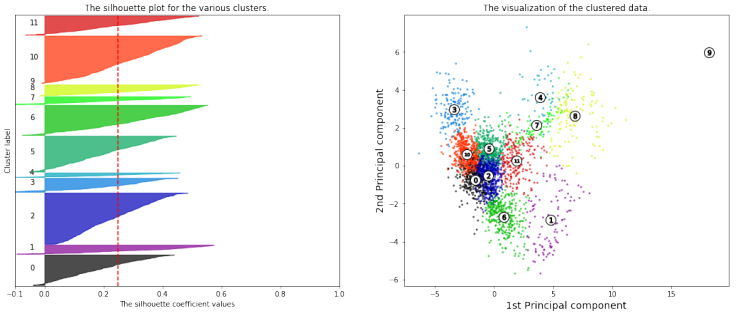


**(e)** Dataset 1: 12 clusters

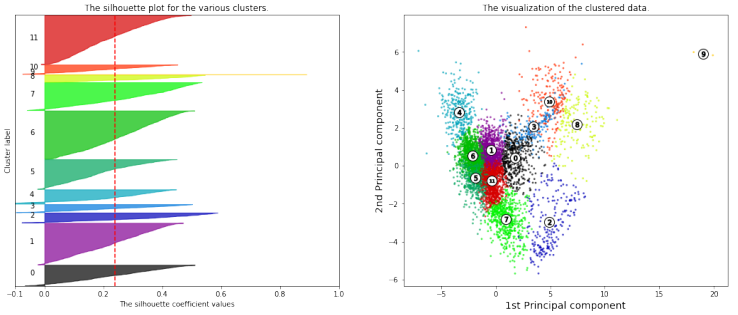


**(f)** Dataset 2: 12 clusters

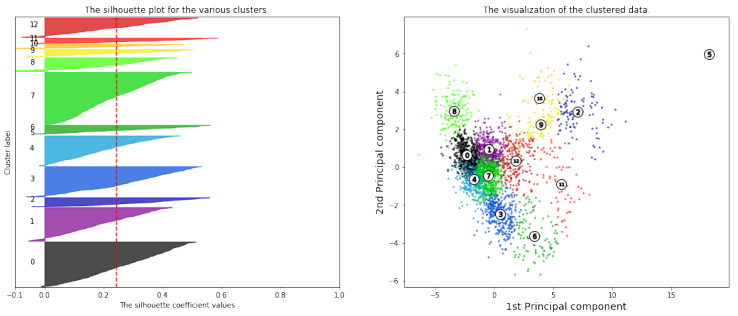


**(g)** Dataset 1: 13 clusters

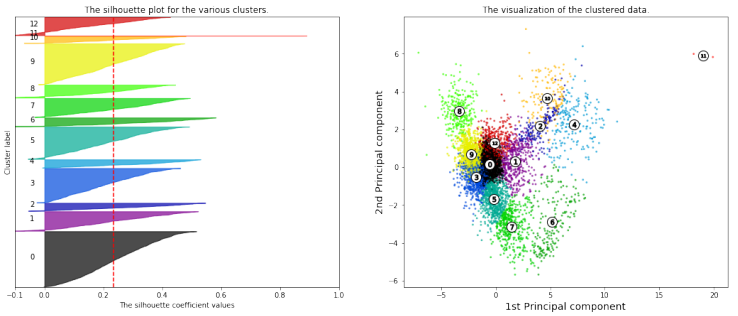


**(h)** Dataset 2: 13 clusters

**Figure 35:** Silhouette plots achieved on two randomly selected dataset of 3000 pixels (4)

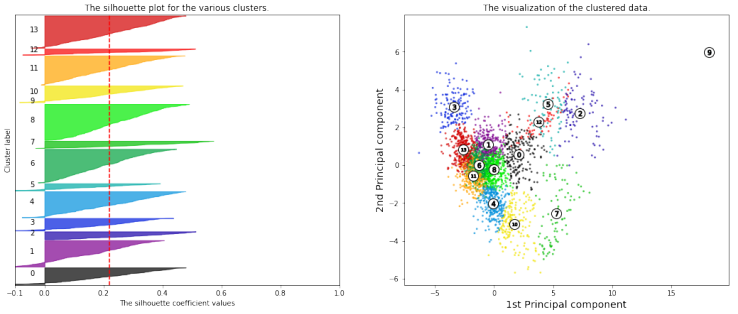


**(a)** Dataset 1: 14 clusters

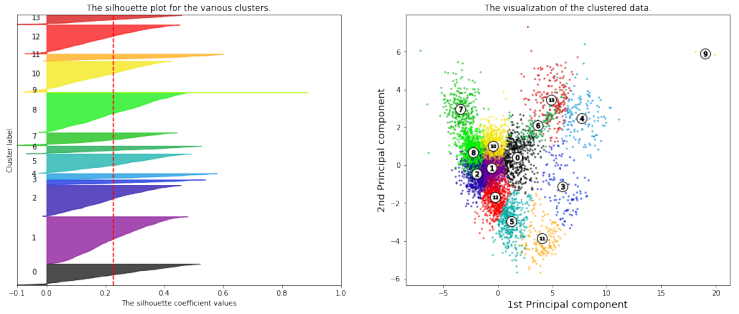


**(b)** Dataset 2: 14 clusters

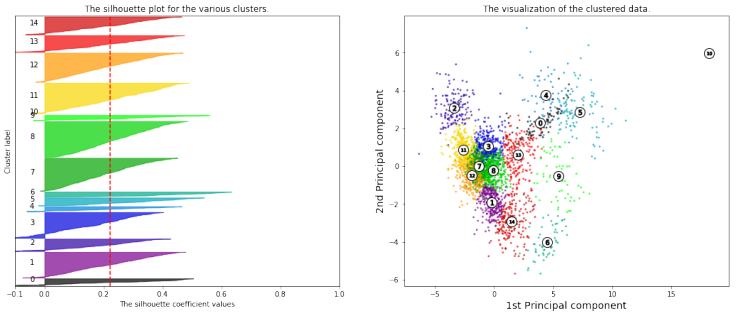


**(c)** Dataset 1: 15 clusters

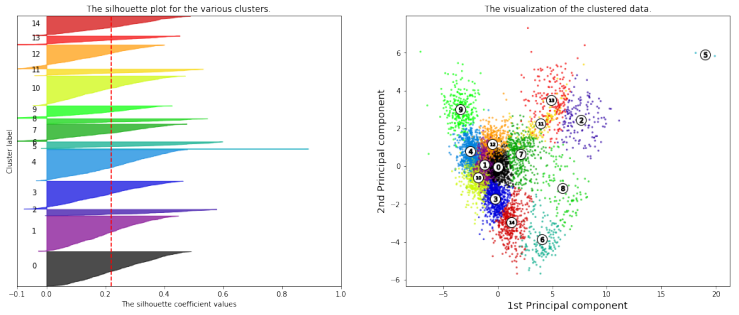


**(d)** Dataset 2: 15 clusters

# References

S. ANDREFOUET, S. MARITORENA, and L. LOUBERSAC. Un bilan de la télédétection appliquée aux milieux coralliens. *Océanis*, 26(3), 2000. ISSN 0182-0745. URL http://archimer.ifremer.fr/doc/00089/20044/.

S. Andrefouet, G. Cabioch, B. Flamand, and B. Pelletier. A reappraisal of the diversity of geomorphological and genetic processes of New Caledonian coral reefs: a synthesis from optical remote sensing, coring and acoustic multibeam observations. *Coral Reefs*, 28(3):691–707, 2009. ISSN 1432-0975. doi: 10.1007/s00338-009-0503-y. URL https://doi.org/10.1007/s00338-009-0503-y.

N. Andrew. CS 229: Machine Learning (Course handouts). Technical report, Stanford, 2015. URL http://cs229.stanford.edu/notes/cs229-notes7a.pdf.

V. E. Brando, J. M. Anstee, M. Wettle, A. G. Dekker, S. R. Phinn, and C. Roelfsema. A physics based retrieval and quality assessment of bathymetry from suboptimal hyperspectral data. *Remote Sensing of Environment*, 113(4):755–770, 2009. ISSN 0034-4257. doi: 10.1016/j.rse.2008.12.003. URL http://www.sciencedirect.com/science/article/pii/S003442570800360X.

H. Buiteveld, J. H. M. Hakvoort, and M. Donze. Optical properties of pure water. volume 2258, pages 174–183, 1994. doi: 10.1117/12.190060. URL http://dx.doi.org/10.1117/12.190060.

L. Buitinck, G. Louppe, M. Blondel, F. Pedregosa, A. Mueller, O. Grisel, V. Niculae, P. Prettenhofer, A. Gramfort, J. Grobler, R. Layton, J. VanderPlas, A. Joly, B. Holt, and G. Varoquaux. API design for machine learning software: experiences from the scikit-learn project. In *ECML PKDD Workshop: Languages for Data Mining and Machine Learning*, pages 108–122, 2013. URL https://orbi.uliege.be/bitstream/2268/154357/1/paper.pdf.

G. Casal, X. Monteys, J. Hedley, P. Harris, C. Cahalane, and T. McCarthy. Optical remote sensing for bathymetry and seabed mapping in the coast of ireland. In *BaSMal*, Brussels, Belgium, November 2017. HIGHROC Science Conference. URL https://cdn.technologynetworks.com/ep/pdfs/optical-remote-sensing-for-bathymetry-and-seabed-mapping-in-the-coast-of-ireland-basmai.pdf.

O. Ceyhun and A. Yalçın. Remote sensing of water depths in shallow waters via artificial neural networks. *Estuarine, Coastal and Shelf Science*, 89(1):89–96, 2010. ISSN 0272-7714. doi: 10.1016/j.ecss.2010.05.015. URL http://www.sciencedirect.com/science/article/pii/S0272771410002088.

A. G. Dekker, S. R. Phinn, J. Anstee, P. Bissett, V. E. Brando, B. Casey, P. Fearns, J. D. Hedley, W. Klonowski, Z. P. Lee, M. Lynch, M. Lyons, C. Mobley, and C. Roelfsema. Intercomparison of shallow water bathymetry, hydro-optics, and benthos mapping techniques in Australian and Caribbean coastal environments. *Limnology and Oceanography: Methods*, 9(9):396–425, 2011. ISSN 1541-5856. doi: 10.4319/lom.2011.9.396. URL http://onlinelibrary.wiley.com/doi/10.4319/lom.2011.9.396/abstract.

A. G. Dekker, S. Sagar, V. E. Brando, and D. Hudson. Bathymetry from satellites for hydrographic purposes. In *6th International Conference on High Resolution Surveys in Shallow*

*Waters*, Wellington, New Zealand, 2012. URL http://www.conference.co.nz/files/docs/shallowsurvey/presentations/26.pdf.

N. Dhanachandra, K. Manglem, and Y. J. Chanu. Image segmentation using k -means clustering algorithm and subtractive clustering algorithm. *Procedia Computer Science*, 54:764 – 771, 2015. ISSN 1877-0509. doi: https://doi.org/10.1016/j.procs.2015.06.090. URL http://www.sciencedirect.com/science/article/pii/S1877050915014143.

T. Duplancic Leder. Satellite derived bathymetry – low cost survey systems. In *7th International Maritime Science Conference*, Solin, Croatia, April 2017. URL https://www.researchgate.net/profile/Tea_Duplancic_Leder/publication/316460253_SATELLITE_DERIVED_BATHYMETRY_-_LOW_COST_SURVEY_SYSTEMS/links/58ff5eff0f7e9bcf65452e64/SATELLITE-DERIVED-BATHYMETRY-LOW-COST-SURVEY-SYSTEMS.pdf.

P. Fua. Computer vision CS-442 | EPFL, Course handouts. Technical report, Lausanne, 2018. URL http://edu.epfl.ch/coursebook/fr/computer-vision-CS-442.

GDAL Development Team. *GDAL - Geospatial Data Abstraction Library, Version x.x.x.* Open Source Geospatial Foundation, 201x. URL http://www.gdal.org.

O. Hagolle, M. Huc, D. V. Pascual, and G. Dedieu. A multi-temporal method for cloud detection, applied to formosat-2, venus, landsat and sentinel-2 images. *Remote Sensing of Environment*, 114(8):1747 – 1755, 2010. ISSN 0034-4257. doi: https://doi.org/10.1016/j.rse.2010.03.002. URL http://www.sciencedirect.com/science/article/pii/S0034425710000908.

S. M. Hamylton, J. D. Hedley, and R. J. Beaman. Derivation of High-Resolution Bathymetry from Multispectral Satellite Imagery: A Comparison of Empirical and Optimisation Methods through Geographical Error Analysis. *Remote Sensing*, 7(12):16257–16273, 2015. doi: 10.3390/rs71215829. URL http://www.mdpi.com/2072-4292/7/12/15829.

H. M. Hassan, Abdelazim M Negm, M. Zahran, and Oliver Saavedra. Assessment of Artificial Neural Network for bathymetry estimation using High Resolution Satellite imagery in Shallow Lakes: Case Study El Burullus Lake. In *International Water Technology Conference*, Sharm ElSheikh, Egypt, March 2015. URL https://www.researchgate.net/publication/273768094_Assessment_of_Artificial_Neural_Network_for_bathymetry_estimation_using_High_Resolution_Satellite_imagery_in_Shallow_Lakes_Case_Study_El_Burullus_Lake.

J. D. Hedley, A. R. Harborne, and P. J. Mumby. Technical note: Simple and robust removal of sun glint for mapping shallow-water benthos. *International Journal of Remote Sensing*, 26 (10):2107–2112, 2005. doi: 10.1080/01431160500034086. URL https://doi.org/10.1080/01431160500034086.

J. D. Hedley, C. Roelfsema, and S. R. Phinn. Efficient radiative transfer model inversion for remote sensing applications. *Remote Sensing of Environment*, 113(11):2527–2532, 2009. ISSN 0034-4257. doi: 10.1016/j.rse.2009.07.008. URL http://www.sciencedirect.com/science/article/pii/S0034425709002314.

J. D. Hedley, C. Roelfsema, B. Koetz, and S. Phinn. Capability of the Sentinel 2 mission for tropical coral reef mapping and coral bleaching detection. *Remote Sensing of Environment*,

120:145–155, May 2012. ISSN 0034-4257. doi: 10.1016/j.rse.2011.06.028. URL http://www.sciencedirect.com/science/article/pii/S0034425712000715.

W. V. Hengel and D. Spitzer. Multi-temporal water depth mapping by means of Landsat TM. *International Journal of Remote Sensing*, 12(4):703–712, 1991. ISSN 0143-1161. doi: 10.1080/01431169108929687. URL http://dx.doi.org/10.1080/01431169108929687.

S. D. Jawak, S. S. Vadlamani, and A. J. Luis. A Synoptic Review on Deriving Bathymetry Information Using Remote Sensing Technologies: Models, Methods and Comparisons. *Advances in Remote Sensing*, 04(02):147, 2015. doi: 10.4236/ars.2015.42013. URL http://www.scirp.org/journal/PaperInformation.aspx?PaperID=57480&#abstract.

T. Kutser and D. L. B. Jupp. On the possibility of mapping living corals to the species level based on their optical signatures. *Estuarine, Coastal and Shelf Science*, 69(3):607–614, 2006. ISSN 0272-7714. doi: 10.1016/j.ecss.2006.05.026. URL http://www.sciencedirect.com/science/article/pii/S0272771406002289.

T. Kutser, A. G. Dekker, and W. Skirving. Modeling spectral discrimination of Great Barrier Reef benthic communities by remote sensing instruments. *Limnology and Oceanography*, 48 (1part2):497–510, 2003. ISSN 1939-5590. doi: 10.4319/lo.2003.48.1_part_2.0497. URL http://onlinelibrary.wiley.com/doi/10.4319/lo.2003.48.1_part_2.0497/abstract.

T. Kutser, I. Miller, and D. L. B. Jupp. Mapping coral reef benthic substrates using hyperspectral space-borne images and spectral libraries. *Estuarine, Coastal and Shelf Science*, 70(3):449–460, 2006. ISSN 0272-7714. doi: 10.1016/j.ecss.2006.06.026. URL http://www.sciencedirect.com/science/article/pii/S0272771406002897.

Laporte, J. SDB DEVELOPMENTS seen from an R & D perspective. In *32nd NORTH SEA HYDROGRAPHIC COMMISSION MEETING*, Dublin, Ireland, June 2016. URL https://www.iho.int/mtg_docs/rhc/NSHC/NSHC32/NSHC32-C.7.1_SDB_ARGANS.pdf.

S. Lê, J. Josse, and F. Husson. FactoMineR: A package for multivariate analysis. *Journal of Statistical Software*, 25(1):1–18, 2008. ISSN 1548-7660. doi: 10.18637/jss.v025.i01. URL http://www.jstatsoft.org/v25/i01/.

Z. Lee, K. L. Carder, C. D. Mobley, R. G. Steward, and J. S. Patch. Hyperspectral remote sensing for shallow waters. I. A semianalytical model. *Applied Optics*, 37(27):6329–6338, 1998a. ISSN 2155-3165. doi: 10.1364/AO.37.006329. URL https://www.osapublishing.org/abstract.cfm?uri=ao-37-27-6329.

Z. Lee, K. L. Carder, C. D. Mobley, R. G. Steward, and J. S. Patch. Hyperspectral remote sensing for shallow waters: 2. Deriving bottom depths and water properties by optimization. *Applied Optics*, 38(18):3831–3843, 1999. ISSN 2155-3165. doi: 10.1364/AO.38.003831. URL https://www.osapublishing.org/abstract.cfm?uri=ao-38-18-3831.

Z. P. Lee, M. R. Zhang, K. L. Carder, and L. O. Hall. A neural network approach to deriving optical properties and depths of shallow waters. In *Proceedings, Ocean Optics XIV*, Kailua-Kona, 1998b. Office of Naval Research, Washington, DC. URL http://faculty.umb.edu/zhongping.lee/Files/Lee_1998_NN.pdf.

S. Liu, Y. Gao, W. Zheng, and X. Li. Performance of two neural network models in bathymetry. *Remote Sensing Letters*, 6(4):321–330, 2015. ISSN 2150-704X. doi: 10.1080/2150704X.2015.1034885. URL http://dx.doi.org/10.1080/2150704X.2015.1034885.

L. Louvart. SATELLITE DERIVED BATHYMETRY Coastal mapping update. In *32nd NORTH SEA HYDROGRAPHIC COMMISSION MEETING*, Dublin, Ireland, June 2016. URL https://www.iho.int/mtg_docs/rhc/NSHC/NSHC32/NSHC32-C.6.1a_SHOM_SDB.pdf.

D. R. Lyzenga. Passive remote sensing techniques for mapping water depth and bottom features. *Appl. Opt.*, 17(3):379–383, February 1978. doi: 10.1364/AO.17.000379. URL http://ao.osa.org/abstract.cfm?URI=ao-17-3-379.

D. R. Lyzenga. Remote sensing of bottom reflectance and water attenuation parameters in shallow water using aircraft and landsat data. *International Journal of Remote Sensing*, 2(1):71–82, 1981. doi: 10.1080/01431168108948342. URL https://doi.org/10.1080/01431168108948342.

D. R. Lyzenga, N. P. Malinas, and F. J. Tanis. Multispectral bathymetry using a simple physically based algorithm. *IEEE Transactions on Geoscience and Remote Sensing*, 44(8):2251–2259, August 2006. ISSN 01962892. doi: 10.1109/TGRS.2006.872909. URL http://ieeexplore.ieee.org/document/1661813/.

P. Maheswary and N. Srivastava. Retrieval of Remote Sensing Images Using Colour and Texture Attribute. *arXiv:0908.4074 [cs]*, 2009. URL http://arxiv.org/abs/0908.4074. arXiv: 0908.4074.

M. Manessa, A. Kanno, M. Sekine, M. Haidar, K. Yamamoto, T. Imai, and T. Higuchi. Satellite-derived bathymetry using random forest algorithm and worldview-2 imagery. *Geoplanning: Journal of Geomatics and Planning*, 3(2):117–126, 2016. ISSN 2355-6544. doi: 10.14710/geoplanning.3.2.117-126. URL https://ejournal.undip.ac.id/index.php/geoplanning/article/view/12047.

M. D. M. Manessa, A. Kanno, M. Sekine, E. E. Ampou, N. Widagti, and A. R. As-syakur. Shallow-water benthic identification using multispectral satellite imagery: Investigation on the effects of improving noise correction method and spectral cover. *Remote Sensing*, 6(5):4454–4472, 2014. ISSN 2072-4292. doi: 10.3390/rs6054454. URL http://www.mdpi.com/2072-4292/6/5/4454.

A. Manuputty, J. L. Gaol, and S. Agus. Seagrass mapping based on satellite image worldview-2 by using depth invariant index method. *ILMU KELAUTAN: Indonesian Journal of Marine Sciences*, 21(1):37–44, 2015. ISSN 2406-7598. doi: 10.14710/ik.ijms.21.1.37-44. URL https://ejournal.undip.ac.id/index.php/ijms/article/view/10042.

A. Manuputty, J. L. Gaol, S. B. Agus, and I. W. Nurjaya. The utilization of depth invariant index and principle component analysis for mapping seagrass ecosystem of kotok island and karang bongkok, indonesia. *IOP Conference Series: Earth and Environmental Science*, 54(1):012083, 2017. URL http://stacks.iop.org/1755-1315/54/i=1/a=012083.

A. Minghelli-Roman and C. Dupouy. Correction of the water column attenuation: Application to the seabed mapping of the lagoon of new caledonia using meris images. *IEEE Journal of Selected Topics in Applied Earth Observations and Remote Sensing*, 7(6):2619–2629, June 2014.

ISSN 1939-1404. doi: 10.1109/JSTARS.2014.2307956. URL http://ieeexplore.ieee.org/document/6775260/.

C. D. Mobley, L. K. Sundman, C. O. Davis, J. H. Bowles, T. V. Downes, R. A. Leathers, M. J. Montes, W. P. Bissett, D. D. R. Kohler, R. P. Reid, E. M. Louchard, and A. Gleason. Interpretation of hyperspectral remote-sensing imagery by spectrum matching and look-up tables. *Applied Optics*, 44(17):3576, 2005. ISSN 0003-6935. doi: 10.1364/AO.44.003576. URL https://www.osapublishing.org/abstract.cfm?URI=ao-44-17-3576.

K. P. Murphy. *Machine Learning: A Probabilistic Perspective*. MIT Press, 2012. ISBN 978-0-262-01802-9. Google-Books-ID: NZP6AQAAQBAJ.

F. Murtagh and P. Legendre. Ward's Hierarchical Agglomerative Clustering Method: Which Algorithms Implement Ward's Criterion? *Journal of Classification*, 31(3):274–295, 2014. ISSN 0176-4268, 1432-1343. doi: 10.1007/s00357-014-9161-z. URL https://link.springer.com/article/10.1007/s00357-014-9161-z.

S. Ouillon, P. Douillet, J. Lefebvre, R. L. Gendre, A. Jouon, P. Bonneton, J. Fernandez, C. Chevillon, O. Magand, J. Lefèvre, P. L. Hir, R. Laganier, F. Dumas, P. Marchesiello, A. B. Madani, S. andrefouet, J. Panché, and R. Fichez. Circulation and suspended sediment transport in a coral reef lagoon: The south-west lagoon of new caledonia. *Marine Pollution Bulletin*, 61(7): 269 – 296, 2010. ISSN 0025-326X. doi: https://doi.org/10.1016/j.marpolbul.2010.06.023. URL http://www.sciencedirect.com/science/article/pii/S0025326X10002663. New Caledonia tropical lagoons: an overview of multidisciplinary investigations.

W. D. Philpot. Bathymetric mapping with passive multispectral imagery. *Applied Optics*, 28(8): 1569, 1989. ISSN 0003-6935. doi: 10.1364/AO.28.001569. URL https://www.osapublishing.org/abstract.cfm?URI=ao-28-8-1569.

R. M. Pope and E. S. Fry. Absorption spectrum (380–700 nm) of pure water II Integrating cavity measurements. *Applied Optics*, 36(33):8710, 1997. ISSN 0003-6935. doi: 10.1364/AO.36.008710. URL https://www.osapublishing.org/abstract.cfm?URI=ao-36-33-8710.

P. J. Rousseeuw. Silhouettes: A graphical aid to the interpretation and validation of cluster analysis. *Journal of Computational and Applied Mathematics*, 20:53–65, 1987. ISSN 0377-0427. doi: 10.1016/0377-0427(87)90125-7. URL http://www.sciencedirect.com/science/article/pii/0377042787901257.

R. P. Stumpf, K. Holderied, and M. Sinclair. Determination of water depth with high-resolution satellite imagery over variable bottom types. *Limnology and Oceanography*, 48(1part2):547–556, 2003. ISSN 1939-5590. doi: 10.4319/lo.2003.48.1_part_2.0547. URL http://onlinelibrary.wiley.com/doi/10.4319/lo.2003.48.1_part_2.0547/abstract.

L. Sun, X. Mi, J. Wei, J. Wang, X. Tian, H. Yu, and P. Gan. A cloud detection algorithm-generating method for remote sensing data at visible to short-wave infrared wavelengths. *ISPRS Journal of Photogrammetry and Remote Sensing*, 124:70 – 88, 2017. ISSN 0924-2716. doi: https://doi.org/10.1016/j.isprsjprs.2016.12.005. URL http://www.sciencedirect.com/science/article/pii/S0924271616306189.

D. Team. THE BENEFITS OF THE EIGHT SPECTRAL BANDS OF WORLDVIEW-2, 2010. URL https://dg-cms-uploads-production.s3.amazonaws.com/uploads/document/file/35/DG-8SPECTRAL-WP_0.pdf.

R. Tibshirani. Statistics 36-350: Data Mining : Lecture 8: Distances between Clustering, Hierarchical Clustering. Technical report, Carnegie Mellon University, Pittsburgh, 2009. URL http://www.stat.cmu.edu/~cshalizi/350/lectures/08/lecture-08.pdf.

C.-K. Wang and W. D. Philpot. Using airborne bathymetric lidar to detect bottom type variation in shallow waters. *Remote Sensing of Environment*, 106(1):123 – 135, 2007. ISSN 0034-4257. doi: https://doi.org/10.1016/j.rse.2006.08.003. URL http://www.sciencedirect.com/science/article/pii/S0034425706003002.

M. Wettle and V. E. Brando. SAMBUCA - Semi-analytical model for Bathymetry, un-mixing and concentration assessment. 2006. doi: https://doi.org/10.4225/08/5866a187b7a3c. URL https://publications.csiro.au/rpr/pub?list=BRO&pid=procite:ba934f66-2eb4-4a69-8782-b19c0e9ecf72.

Wikipedia. Algebraic formula for the variance, 2015. URL https://en.wikipedia.org/w/index.php?title=Algebraic_formula_for_the_variance&oldid=648447331. Page Version ID: 648447331.